phys. stat. sol. (c) **1**, No. 8, 2028–2055 (2004) / DOI 10.1002/pssc.200404762

Optical properties of low-dimensional semiconductor systems fabricated by cleaved edge overgrowth

R. Schuster[*1], **H. Hajak**[1], **M. Reinwald**[1], **W. Wegscheider**[1], **G. Schedelbeck**[2], **S. Sedlmaier**[2], **M. Stopa**[**2], **S. Birner**[2], **P. Vogl**[2], **J. Bauer**[2], **D. Schuh**[2], **M. Bichler**[2], and **G. Abstreiter**[2]

[1] Institut für Experimentelle und Angewandte Physik, Universität Regensburg, 93040 Regensburg, Germany
[2] Walter Schottky Institut, Technische Universität München, Am Coulombwall, 85748 Garching, Germany

Received 15 March 2004, revised 6 May 2004, accepted 13 May 2004
Published online 23 June 2004

PACS 73.20.At, 73.21.Hb, 73.21.La, 78.45.+h, 78.67.Hc 78.67.Lt

An overview of the cleaved edge overgrowth technique, which allows the realization of atomically precise quantum structures, is presented. We explain the origin of the formation of quantum wires, which were grown with this molecular beam epitaxy method. The emission of quantum wire lasers based on these intrinsic T-shaped structures shows a strong dependence on magnetic fields. Only weak band gap renormalization is observed for modulation doped wires when the electron density is varied. The introduction of strained layers results in an enhancement of the confinement energy, which is necessary to fully exploit the one-dimensional character of the examined quantum wires. Single as well as coupled quantum dots, and quantum dot superlattices have been successfully grown and are identified using micro-photoluminescence spectroscopy. By combining self-assembling of quantum dots due to Stranski-Krastanov growth with the cleaved edge overgrowth method we succeeded in fabricating arrays of long-range ordered InAs quantum dots. Both atomic force microscopy and micro-photoluminescence measurements performed on such samples show the ability to control size, position, and ordering of the quantum dots.

© 2004 WILEY-VCH Verlag GmbH & Co. KGaA, Weinheim

1 Introduction

The breakthrough of 2D semiconductor systems for optical and transport applications like quantum well (QW) lasers, intersubband detectors or high electron mobility transistors was triggered by the development of highly sophisticated growth techniques like molecular beam epitaxy (MBE). Although these techniques are well suited to produce planar multilayer systems with interfaces which are flat on an atomic scale, the fabrication of structures in which charge carriers are quantum confined in more than one dimension remains a challenging task. Methods suggested and attempted include lithographic definition combined with etching and regrowth [1], growth on nonplanar [2] and vicinal substrates [3, 4], selective area deposition [5], and local interdiffusion [6, 7]. The pattern transfer by lithographic techniques introduces size fluctuations which blur most of the effects caused by the reduced dimensionality. Self-organisation has proven to be a powerful technique for the preparation of quantum wires (QWRs) which form after organometallic chemical vapor deposition (OMCVD) on V-grooved substrates [2]. However, the relatively large size of the crescent-shaped QWRs (80-100 by 10 nm) which were achievable by this technique in the first experiments resulted in the occupation of more than one 1D subband, and therefore in optical properties reminescent to those of 2D systems. The realization of quantum dots (QDs) using this approach was also demonstrated when the deposition was carried out on pyramidal recess patterns etched into GaAs $\{111\}$B

* Corresponding author: e-mail: robert.schuster@physik.uni-regensburg.de, Phone: +49 941 943 2066, Fax: +49 941 943 4226
** Present address: ERATO-JST, 4S-308S, NTT Atsugi Research and Development Laboratories, 3-1 Morinosato-Wakamiya, Atsugi-shi Kanagawa-ken, 243-0198, Japan.

© 2004 WILEY-VCH Verlag GmbH & Co. KGaA, Weinheim

substrates [8]. For these structures subband spacings of more than 30 meV and photoluminescence (PL) linewidths $<$ 15 meV in 2D arrays have been achieved [9].

Today, In(Ga)As and In(Al)As dot layers in GaAs or AlAs can be grown by MBE with reasonably well defined emission energy, dot density, and high size homogeneity (e.g. [10]). However, to date it is much more difficult to controllably position individual self-assembled QDs on the growth surface. One possible approach is to exploit modified growth kinetics that occurs on high index vicinal surfaces with regularly ordered atomic steps. Examples of such novel approaches include In(Ga)As QDs and QWRs grown on GaAs (311)A [11], on miscut (100)-oriented GaAs [12] or at crystal defects [13]. Another approach is to use lithographically patterned substrates to force controlled dot nucleation (e.g. [14, 15]). All these methods are either based on intrinsic substrate properties and are, therefore, not very flexible or are limited by the lithographic technique used.

This article gives an overview of another method for the fabrication of QWRs and QDs which makes use of MBE growth on atomically flat cleavage planes of previously prepared multilayer structures. This so-called cleaved edge overgrowth (CEO) technique enables us to prepare quantum size structures with characteristic dimensions down to a few lattice constants. This turns out to be of particular importance since the peculiar features associated with 1D excitons predicted by theory [16, 17] can be only observed if the QWR dimensions are comparable or smaller than the bulk exciton Bohr radius. Otherwise only the center-of-mass motion of the excitons shows 1D character while the electron-hole relative motion remains unaffected. In additon, arrays of QWRs and QDs fabricated by CEO are very uniform in size comparable to the homogeneity achievable in multiple quantum well (MQW) layers. This is advantageous for laser applications where a large number of QWRs or QDs are necessary but should not degrade device performance because of size fluctuation induced broadening of the gain spectra.

2 Cleaved edge overgrowth

The concept of CEO is illustrated in Fig. 1. The conceptually simple and straightforward approach consists of two or three growth steps separated by an *in situ* cleavage. The cleavage process has to be performed in an ultrahigh vacuum environment, since exposure of the highly reactive Al containing layers to air is accompanied by the formation of a stable oxide which cannot be thermally desorbed. In order to avoid contamination of the (110) cleavage face by impurities from the residual gas atmosphere, the time between the cleavage and the initiation of overgrowth should be as short as possible. The fabrication of a complete CEO structure, successfully realized for the first time by Pfeiffer *et al.* [19] is summarized below.

After the first MBE growth the wafer is removed from the MBE machine and thinned from the backside using Br_2CH_3OH to a thickness of 100-150 µm. The thin wafer is then scribed and cleaved into rectangular pieces of about 5 by 10 mm. A scratch is made where the future *in situ* cleavage is to occur. Up to eight of these pieces are mounted next to a GaAs (110) monitor wafer. In this way the (110) surface exposed after the cleavage is parallel to the surface of the monitor wafer. The purpose of the monitor wafer is twofold. It provides a surface of proper emissivity for the measurement of the growth temperature, which turns out to be a critical parameter for GaAs (110) epitaxy, using a pyrometer. In addition it serves as a reference sample for the layer sequence grown after the cleavage which can be more easily characterized than the CEO samples. Similar to conventional substrate introduction the CEO substrate holder assembly is loaded into the growth chamber. After the machine is brought into running condition, the oxide from the (110) monitor wafer is desorbed such that a buffer layer can be grown. Then the cleavage is performed. Within seconds MBE growth is initiated and proceeds both on the newly exposed cleavage as well as on the adjacent monitor wafer. The CEO technique can be applied to the production of a variety of different sample structures suitable for optical and transport investigations. In this article only results of QWRs and QDs obtained by optical spectroscopy are discussed.

© 2004 WILEY-VCH Verlag GmbH & Co. KGaA, Weinheim

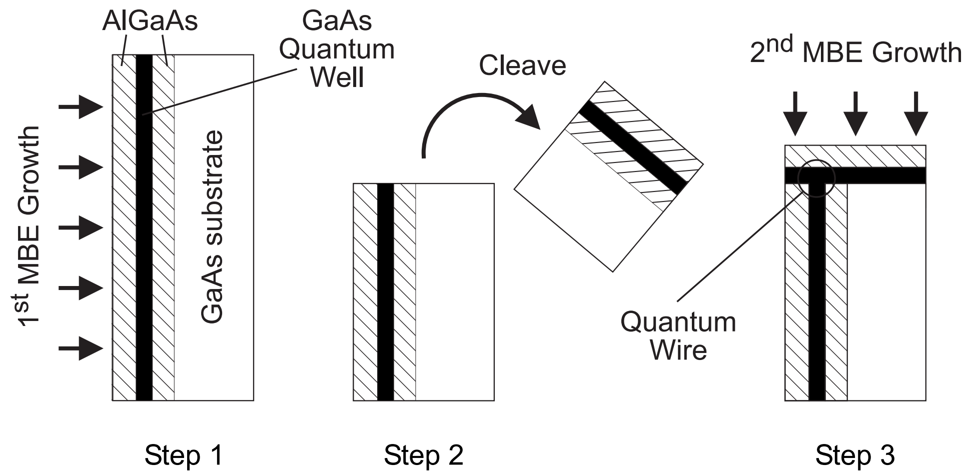

Fig. 1 The concept of cleaved edge overgrowth: Two MBE growth steps, separated by an *in situ* cleavage. After [18].

3 Quantum wires

Figure 2 illustrates the physics of QWR formation at the T-shaped intersection of two quantum wells. The figure shows the cross-section of such an intersection together with contours of constant probability for electrons and holes. The origin of the quantum mechanical bound state is the relaxation of QW confinement at the intersection. While a classical particle would be unbound for the given T-shaped potential, the expansion of the wave function into the larger available volume at the junction results in a smaller kinetic contribution to the total energy of electrons and holes. Consequently, motion of the 1D carrier is limited to the line defined by the intersecting planes of the two QWs.

In contrast to other QWR fabrication techniques which introduce additional confinement of the carriers in a previously prepared 2D system, for example by partial removal of a QW layer and subsequent overgrowth with barrier material, the QWR states in this structure are energetically located below the ground state QW transitions. The existence of such confinement relaxation QWR states was proposed about twenty years ago by Chang *et al.* [21]. The intersection of three QWs can be realized by another cleavage step followed by overgrowth. Analogous to the formation of 1D states at the intersection of two QWs, carriers in such QDs are quantum confined in all 3 dimensions and a QD forms. Such structures have been first realized by Wegscheider *et al.* [22] and Schedelbeck *et al.* [23]. Localization energies of the ground state excitons in such QDs have been calculated by Grundmann and Bimberg [24].

3.1 Theory

The theoretical treatment of quantum confined states at the intersection of two QWs requires solving of the two-dimensional Schrödinger equation for the T-shaped potential. Although simplified calculations [21, 25] based on factorization of the structure potential, thus, reducing the problem to an effective one-dimensional Schrödinger equation, give physical insight and lead to analytical results, they are not accurate enough for this purpose. Figure 2(a) shows the electron probability density $|\psi|^2$ of the electron ground state for a structure with two 7 nm wide GaAs QWs embedded in $Al_{0.35}Ga_{0.65}As$ barrier material obtained by the free-relaxation method where an anisotropic effective mass and nonparabolicity can be included [26]. Evidently, the wave function ψ differs strongly from a factorizable one.

In order to predict transition energies of interband QWR transitions hole confinement and also excitonic effects have to be included. Although sophisticated calculations for the valence band using a $\mathbf{k}\cdot\mathbf{p}$ model

© 2004 WILEY-VCH Verlag GmbH & Co. KGaA, Weinheim

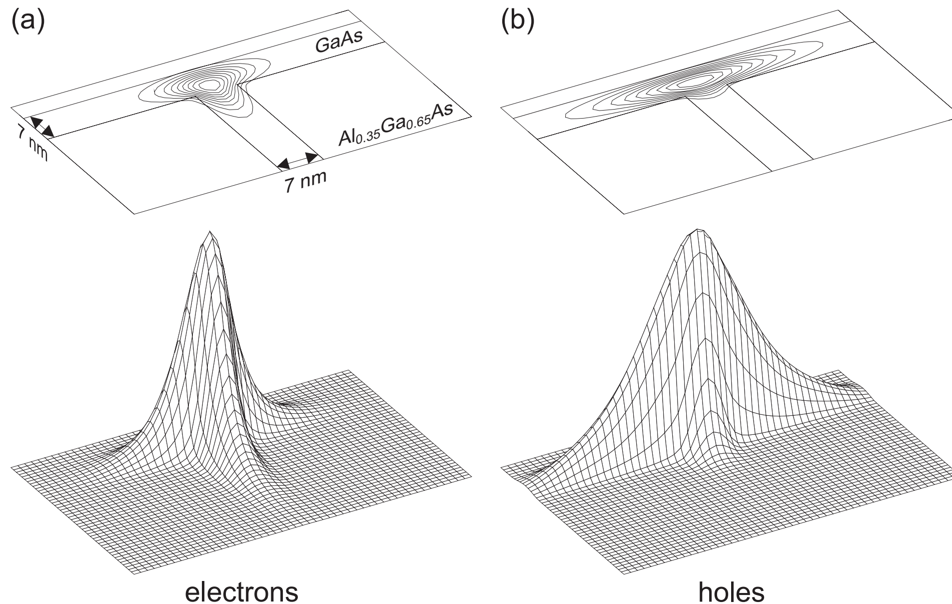

Fig. 2 The electron (a) and hole (b) probability density for the wire-like state in the GaAs/$Al_{0.35}Ga_{0.65}As$ T-shaped structure with 7 nm wide wells. After [20].

which includes six bands and, thus, mixing of the heavy-hole, light-hole, and split-off hole, have been carried out [27, 28], the small heavy-hole binding energies of less than 2 meV are very well reproduced by a simple one-band calculation with masses determined via the diagonal term in the Luttinger Hamiltonian with the angular momentum quantization axis parallel to the [110] overgrowth direction. As a result of the heavy-hole mass dependence on the crystallographic direction the eigenvalues for the two QWs are different and the holes are for equal well widths much more spread out into the overgrown QW as can be seen in Fig. 2(b).

In addition to factorization and variational methods applied to the exciton problem in T-shaped QWRs [26, 29, 30] an accurate numerical solution for the ground state of the two-particle problem has been developed [31]. In contrast to the interaction-free case the Coulomb-correlated hole is found to be strongly localized. The authors demonstrated that one-dimensional hole confinement is not necessary for the formation of a one-dimensional exciton and that a two-dimensional-hole, bound to a one-dimensional electron, is a good approximation for an exciton in a T-QWR.

3.2 Magnetic field dependence of the quantum wire emission

The first attempts to study the operation of QWR and quantum box lasers were based on Landau quantization of carriers [32, 33]. As a result of Lorentz force confinement electrons and holes in heterostructure lasers can move freely only in the direction of the magnetic field and quasi-QWR structures are obtained. Accordingly, application of a magnetic field in the growth direction of a QW laser leads to full quantization of the charge carriers and the properties of 0D lasers can be simulated. In agreement with theory these experiments indeed demonstrate a reduced temperature sensitivity of the threshold current [32, 34] as well as an enhanced modulation bandwidth [35], and a reduction of the spectral linewidth [36, 37]. However, the emitted intensity and the threshold current of the lasers were almost unaffected by the application of magnetic fields up to $B = 30$ T.

We studied 1D lasers incorporating QWR potential wells as fabricated by the CEO method under strong magnetic fields oriented parallel and perpendicular to the QWR axis. A schematic view of the QWR

© 2004 WILEY-VCH Verlag GmbH & Co. KGaA, Weinheim

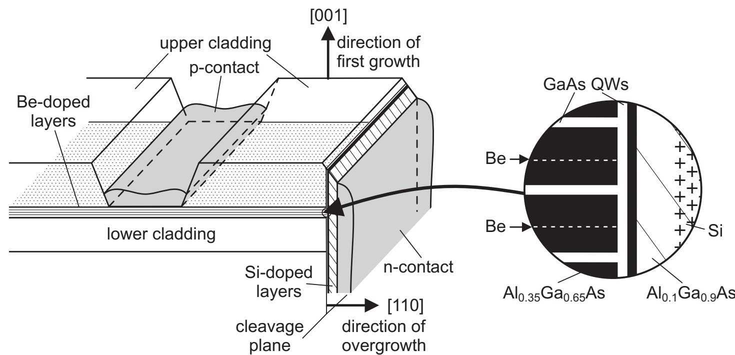

Fig. 3 Schematic representation of the QWR laser diode (not to scale). After [20].

structure, which is identical to that studied in Ref. [38] in the absence of a magnetic field, is shown in Fig. 3. The first MBE growth on a (001) GaAs semi-insulating substrate consists of a 0.5 µm GaAs buffer layer, a 1 µm $Al_{0.5}Ga_{0.5}As$ lower cladding layer, a 15-period GaAs/$Al_{0.35}Ga_{0.65}As$ MQW structure with well and barrier thicknesses of 7 and 58 nm, followed by a 3 µm $Al_{0.5}Ga_{0.5}As$ upper cladding layer and 10 nm GaAs cap. Be doping spikes (2×10^{11} Be cm^{-2}) are located in each $Al_{0.35}Ga_{0.65}As$ barrier 34 nm below and 24 nm above each QW (see magnified portion of Fig. 3). The post-cleavage growth sequence consists of a 7 nm GaAs QW (undoped) followed by a 7 nm $Al_{0.35}Ga_{0.65}As$ barrier (undoped), a 43 nm undoped $Al_{0.1}Ga_{0.9}As$ setback, a l24 nm doped $Al_{0.1}Ga_{0.9}As$ layer (2×10^{18} Si cm^{-3}), a 1 µm wide $Al_{0.5}Ga_{0.5}As$ cladding layer (2×10^{18} Si cm^{-3}) and a 10 nm GaAs cap (2×10^{18} Si cm^{-3}). The cladding layers and the $Al_{0.1}Ga_{0.9}As$ layer serve as a T-shaped dielectric waveguide confining an optical mode in the vicinity of the QWR array [39]. In order to contact the p-doped QWs the upper cladding layer was partially etched away as shown schematically in Fig. 3. AuBe and AuGe were used for the p- and n-type ohmic contacts, respectively. After metallization the samples were again cleaved so as to form optical cavities bound by mirrors perpendicular to the axis of the QWRs. The cleave mirrors were left uncoated so that each mirror had a reflectivity R of only about 0.3. The measurements were performed in a He storage dewar (T = 4.2 K) or a commercial ^{3}He system (T = 370 mK) equipped with a superconducting magnet. Light emitted from continuously operated laser diodes was transmitted through an optical fiber and either dispersed in a double monochromator or focused onto a Si photodiode detector. The low temperature regime was chosen in order to prevent the thermal excitation of charge carriers from the QWR to the QW states, from which they are separated only by a relatively small confinement energy. However, lasing from a single QWR at 60 K has already been observed [40].

Figure 4(a) shows the evolution of the light output from the 400 µm long T-QWR diode laser with increasing magnetic field for a field direction parallel to the axis of the QWRs. For $B = 0$ T the light versus current (L/I) characteristic of this device deviates only weakly from a strictly linear relationship. With increasing magnetic field the emitted light intensity above this threshold current (I_{th}) shows a pronounced increase of about a factor of 8 for the highest magnetic field of $B = 12$ T at 1 mA injection current and clear superlinear behavior is observed. At the same time the electrical diode characteristic of the device remains unaffected by the application of the magnetic field. A more detailed measurement of the L/I characteristics in the vicinity of the threshold current of about 0.4 mA is shown in Fig. 4(b). Again, an increase in the emitted intensity above threshold can be seen. However, all L/I curves cross at about 0.4 mA, i.e. light emission is reduced for currents $I < I_{th}$, and is enhanced for currents $I > I_{th}$. In order to understand this behavior the L/I characteristic have been simulated using a standard rate equation model [42], modified for a laser which operates from localized excitons, which are bound at minima in the QWR potential [41]:

© 2004 WILEY-VCH Verlag GmbH & Co. KGaA, Weinheim

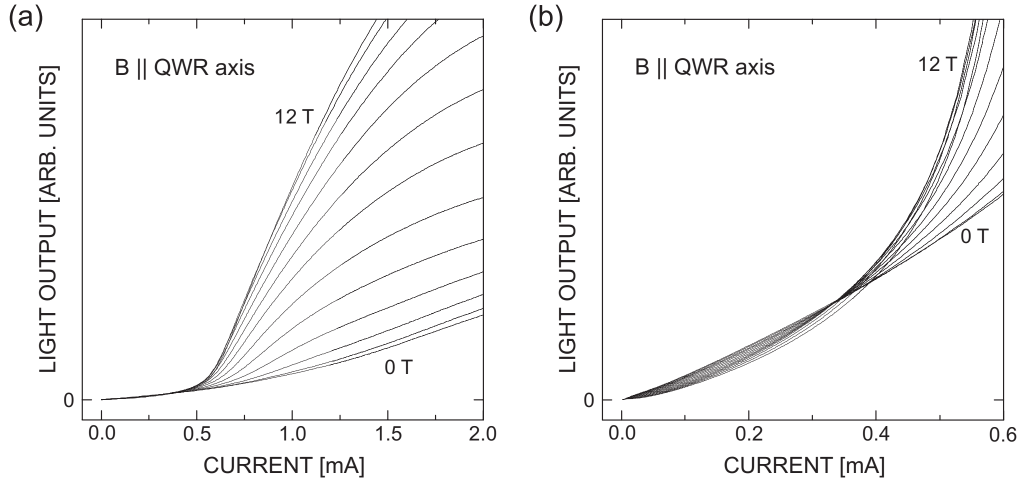

Fig. 4 Light vs. current characteristic of a 400 µm long QWR laser in a magnetic field oriented parallel to the QWR axis. The magnetic field was increased from $B = 0$ to 12 T in increments of 1 T. After [41].

$$\frac{\mathrm{d}}{\mathrm{d}t}n = \frac{I(1-n)}{qN} - \frac{Gn}{\beta} - GP(2n-1) - \gamma n, \tag{1}$$

$$\frac{\mathrm{d}}{\mathrm{d}t}P = P[GN(2n-1) - \kappa] + GNn, \tag{2}$$

where n is the average occupancy of the bound exciton level which lases, q is the elementary charge, N is the density of states of such levels, GN is the total gain, β is the fraction of spontaneous emission coupling to the cavity, P is the number of photons in the lasing mode, γ is the non-radiative recombination rate, and κ is the cavity loss rate. In contrast to a conventional laser where the increase in the number of inverted levels is proportional to the current I, pumping has been written as $I(1-n)/qN$. This is due to the fact that more than two excitons cannot be localized on the same site. Solving the steady state behavior ($\mathrm{d}/\mathrm{d}t = 0$) of the rate equations, (1) and (2) reduce to a quadratic equation with the solution (written here for $\gamma = 0$):

$$P(i) = \frac{1}{4g}\left\{(g-1)(i-i_{th}) + \left[(g-1)^2(i-i_{th})^2 + 8g^2 i\right]^{1/2}\right\}, \tag{3}$$

where the "threshold" current

$$i_{th} = \frac{g^2 + g - \beta g^2}{\beta(g-1)}, \tag{4}$$

the dimensionless gain $g = GN/\kappa$ and current $i = I/q\kappa$ have been introduced. Notice that there is no threshold for $g < 1$. Since overall gain can only be obtained for $g(2n-1) > 1$ [eqn (2)], this is simply a consequence of the restriction $n < 1$. In the low and high current limits eqn (3) reduces to

$$P(i) = \frac{\beta i}{g+1} \quad \text{for} \quad i \ll i_{th}, \tag{5}$$

$$P(i) = \frac{i(g-1)}{2g} \quad \text{for} \quad i \gg i_{th}. \tag{6}$$

For a laser which operates just above the transparency criterion ($g \gtrsim 1$), a small increase in g has a strong effect on the light output. In particular, with increasing g the emission goes down below threshold, but

© 2004 WILEY-VCH Verlag GmbH & Co. KGaA, Weinheim

increases above threshold and then saturates. Figure 5 shows the results of changing g from $g = 1$ to 2 in increments of 0.1 using $\beta = 10^{-2}$. The results of the simulation are very similar to the measured L/I curves shown in Fig. 4.

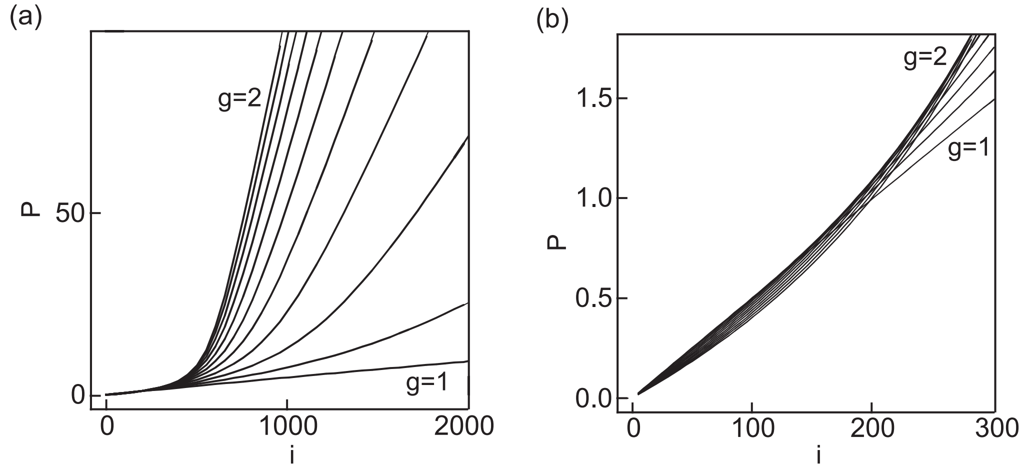

Fig. 5 Calculated number of photons P in the lasing mode vs. the dimensionless current i as a function of the dimensionless gain g, varied from 1 to 2 in increments of 0.1 for an excitonic laser. The relevant parameters entering the calculations are $\gamma = 0$ for the non-radiative recombination rate and $\beta = 10^{-2}$ for the spontaneous emission coupling factor. After [41].

This strongly suggests that the effect of a strong magnetic field applied parallel to the QWR axis is to modulate the gain. This is equivalent to an increase of the oscillator strength for the transitions between the 1D states. However, since confinement of excitons to 1D is already present at $B = 0$ as a result of the T-shaped potential in our samples, substantial effects due to magnetic confinement can be only expected if the cyclotron radius becomes comparable to the exciton Bohr radius of about 10 nm. The observed incremental increase in the laser emission is maximal for a field strength of about 6 T, a value which indeed corresponds to a magnetic length of $(\hbar/eB)^{1/2} = 10$ nm. For higher fields the effect saturates as predicted by theory. This saturation of total gain $GN = gnN$ is a peculiarity which arises from the excitonic nature of the emission in our laser. Without the blocking effect expressed by $I(1-n)/qN$ in eqn (1) the light output is only weakly influenced by changes in gain. In particular, in an “ideal” laser, above threshold the differential slope of the L/I curve is independent of the gain since all the current is converted to light.

For a magnetic field orientation along the direction of overgrowth ([110]), i.e. perpendicular to the QWR axis, a completely different behavior is observed. The corresponding L/I curves recorded on the same sample are shown in Fig. 6. In this case the emitted intensity is already doubled for $B = 1$ T, a field strength which has only little effect on the laser characteristic in the parallel magnetic field configuration (see Fig. 4). Magnetic fields exceeding 4 T, however, are not accompanied by an appreciable increase in the light output for this field direction. In addition, the behavior of the QWR laser below threshold is different as can be seen in more detail in Fig. 6(b). Up to $B = 6.5$ T the light output increases. At higher fields, crossing of the L/I curves is observed. Although the emission intensity starts to decrease for such strong magnetic fields, its absolute value always exceeds the $B = 0$ T value. Similar to the parallel magnetic field configuration the electrical diode characteristic of the device remains unaffected by the application of the magnetic field. Following our argumentation to interpret the results obtained with the magnetic field applied in the direction of the QWR axis, it is very unlikely that the pronounced increase in the emission intensity at low magnetic fields is due to magnetic confinement. In addition, according to our model the increase in light output observed below threshold contradicts an increase in gain.

© 2004 WILEY-VCH Verlag GmbH & Co. KGaA, Weinheim

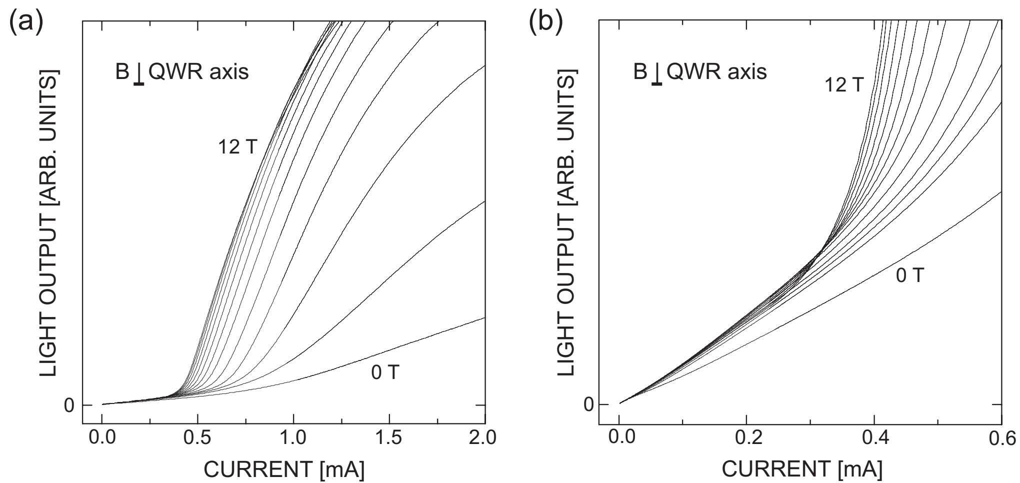

Fig. 6 Light vs. current characteristic of the same laser studied in the parallel magnetic field configuration (see Fig. 4) using a magnetic field direction along the [110] overgrowth direction, i.e. perpendicular to the QWR axis. The magnetic field was increased from $B = 0$ to 12 T in increments of 1 T. After [41].

An alternative approach to describe these results must rely on a mechanism which leads to a more efficient pumping of localized 1D exciton states, which then can radiatively recombine and emit more light at all injection levels. One possibility would be the interaction of the electron and hole spins with the magnetic field. Under the assumption that the electrons and holes generated by current injection are initially not spin polarized, the proportion of singlet (1S) to triplet excitons ($2P^0$, $2P^-$, $2P^+$) in the QWRs should be roughly 1:4. Since only the singlet excitons are optically active, changes in the relative populations induced by the Zeeman effect would also influence the light output. This would lead to a rescaling of the L/I curves, because for any injection current independent of the laser threshold the emission intensity would either increase or decrease. Such a rescaling behavior, which is characterized by the absence of L/I curve crossings near threshold is observed in the low magnetic field data shown in Fig. 6(b). One problem with this interpretation is, that the splitting in energy between the singlet and triplet states is usually less than $k_B T$, so in thermal equilibrium the changes in population would be small. If the rate of equilibration of the populations was slow compared to the radiative lifetime, a population difference, large enough to explain the increase in the emission intensity, might result. The spin-flip times which are only known for 2D systems are factors of 2 to 4 shorter than the radiative lifetime [43, 44]. In the absence of a calculation of the electron Landé g-factors for the two magnetic field orientations in the QWR structure and a reliable value for the spin-flip time it is, however, difficult to judge the validity of our interpretation. Interestingly, this effect should not be observable in conventional 2D lasers which operate in the regime of a degenerate electron-hole plasma, where the spin-flip rates are so fast that spin effects are unimportant. Another possibility to explain the increase in emission with applied magnetic field would be the suppression of carrier diffusion along the wire axis. While for a magnetic field direction parallel to the QWR axis the cyclotron orbits are located in a plane perpendicular to this axis, cyclotron motion for a magnetic field orientation along the direction of overgrowth inhibits free carrier transport along the QWR axis. Since the operation of our T-QWR laser critically depends on the presence of localized excitons this effect which supports the formation of such excitons should also influence the laser characteristic of the device.

Additional investigations performed on structures without a resonator revealed that these systems — operated in absence of lasing — behave similarly when they are subject to a magnetic field. These measurements lead to the conclusion that the observed dependence on the magnetic field is a 1D property of

© 2004 WILEY-VCH Verlag GmbH & Co. KGaA, Weinheim

the systems and cannot be explained by strong nonlinearities above threshold [45]. However, in order to elucidate the nature of the unusual behavior of the T-QWR lasers under strong magnetic fields, further investigations both experimentally and theoretically have to be performed.

3.3 Band gap renormalization of modulation doped QWRs

The intersection of two QWs as shown Fig. 2 confines both electrons and holes as explained in more detail above and is therefore well suited for interband transition experiments requiring large overlap between the electron and hole wave functions.

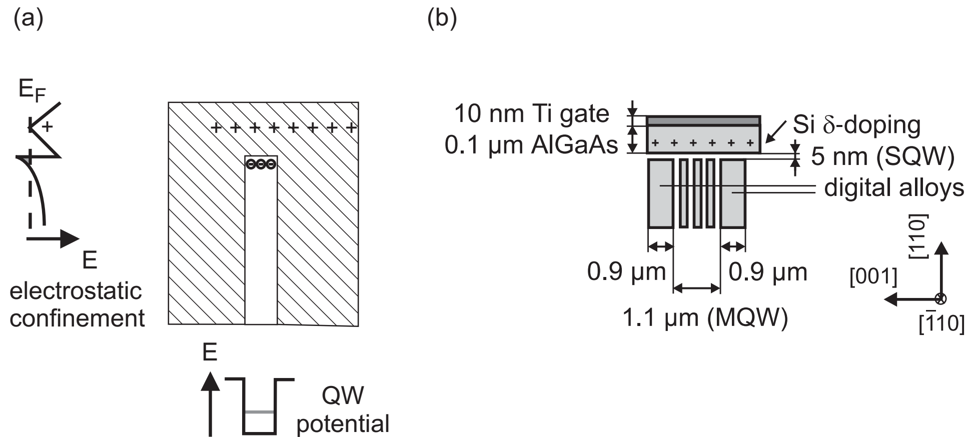

Fig. 7 (a) Modulation-doped QWR. The actual sample schematic is given in (b) showing the multiple, parallel T-shaped QWRs formed at the intersection of the edges of the multiple quantum wells (MQWs) with the single, modulation doped quantum well (SQW) in the overgrowth layer (not true scale). After [46].

A second class of QWRs which represent the 1D analogue to a high-mobility electron layer in 2D is shown in Fig. 7(a). In addition to the electrostatic confinement which arises as a result of charge transfer from the ionized donors over the barrier into the QW, the potential of the latter leads to an electron channel where carrier motion is limited to a line. Magnetotransport measurements on such single modulation doped QWRs are characterized by a retarded depopulation of Landau levels for cyclotron orbits exceeding the width of the confining QW potential [47]. These results are well described by a theoretical model employing a square-well confining potential in the lateral direction of the QWR [48].

Exchange and correlation in an electron gas formed in a semiconductor act to counter the direct Coulomb interaction by reducing the interparticle overlap. For two-component systems, such as the electron-hole plasma created in optical experiments, this effect tends to produce a band gap renormalization (BGR) with increasing density n_e and/or n_h, which reduces the energy of photons emitted upon recombination from the band edges [49]. Here, we present the evolution of the PL energy in a doped QWR sample whose conduction band electron density n_e can be modulated with the voltage applied to a surface gate. Our structure consists of 22 periods of (001)-oriented GaAs (5 nm) / $Al_{0.32}Ga_{0.68}As$ (44 nm) MQWs, grown between two digital alloys with 90 periods of GaAs (2 nm) / $Al_{0.32}Ga_{0.68}As$ (8 nm) each. These digital alloys permit us to observe the PL from the overgrowth single quantum well (SQW), which is defined by growing along the [110]-crystal axis 5 nm GaAs, a 30 nm $Al_{0.35}Ga_{0.65}As$ spacer, a silicon δ-doping (n-modulation doping), and 70 nm $Al_{0.35}Ga_{0.65}As$. After both growth steps, 10 nm thick cap layers are added, which are not included in Fig. 7(b).

In order to interpret the PL line shape of the n-modulation doped QWRs, we compare it with the line shape of intrinsic T-shaped QWRs, as shown in Fig. 8 (the curves are aligned horizontally so that the peaks coincide). Interface roughness, particularly in the (110)-oriented SQW [50], results in an inhomogeneously

© 2004 WILEY-VCH Verlag GmbH & Co. KGaA, Weinheim

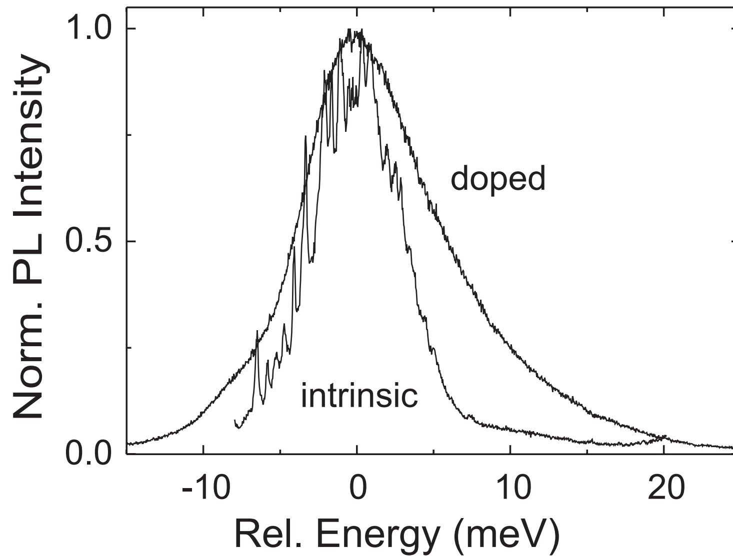

Fig. 8 Comparison between the normalized PL line shapes of intrinsic and n-modulation doped T-shaped QWRs ($n \approx 1 \times 10^6$ cm^{-1}). In order to detect only the QWRs PL and to avoid an overlap with the SQW PL, excitation is performed on the (110) surface. The excitation power amounts to 1 µW, the excitation energy to 1656 meV. After [46].

broadened, on average symmetric PL line of the intrinsic QWRs. The spectrally sharp peaks on the PL line are attributed to excitons localized at monolayer potential fluctuations [51]. In the presence of free carriers, however, this signature of bound excitons vanishes, indicating exciton delocalization or density dependent damping.

Applying a negative gate voltage relative to the electron system, the charge density in the QWRs and in the SQW is reduced. In this way, it is possible to study the energetic position of the PL peak as a function of the charge density. In Fig. 9 one notices a characteristic redshift for the SQW of about $5 - 6$ meV as the 2D electron density n_e is increased form zero to about 2×10^{11} cm^{-2}. The principle result of Fig. 9, however, is the weak variation of the peak position for the QWRs as n_e varies. The overall shift of only about 3 meV, when the electron density is increased from zero to about 1×10^6 cm^{-1}, is similar to results found for wires with a two-component plasma in high excitation [52]. The observation is in excellent agreement with the variation of the band gap determined by the local-density approximation (LDA) calculation when the excitonic screening correction is included. In Fig. 9 we plot the variation of the translationally invariant band edge, the calculated exciton binding energy and the combination of the two as a function of n_e [46]. Clearly, without the screening of the exciton, the band edge variation disagrees markedly with measurement. The variation of the exciton binding, however, is functionally nearly the inverse of the band edge variation, with variation at low n_e strongest in both cases. The result is a close cancellation and a trend with n_e that recapitulates the data. A similar cancellation of exciton binding energy and BGR has been derived by Das Sarma and Wang [53] using the Bethe-Salpeter equation, for the case of a two-component, neutral plasma (i.e. for $n_e = n_h$). However, one striking contrast between our results and those of Ref. [53] is that, up to our highest density $n_e = 3 \times 10^6$ cm^{-1}, we find that the electron and hole remain bound, whereas those authors find a merging of the exciton with the continuum, a so-called Mott transition, in the range of 0.3×10^6 cm^{-1}. The robustness of the exciton revealed in our calculations emerges from the requirement of orthogonality between the free, screening electrons and those bound to the hole; a constraint which is not maintained in the many-body calculation. Therefore, at least in the case of a one-component plasma, we find that the stability of the exciton exceeds that predicted

© 2004 WILEY-VCH Verlag GmbH & Co. KGaA, Weinheim

by the conservative Mott criterion. This result confirms earlier investigations on the properties of T-QWR lasers [39].

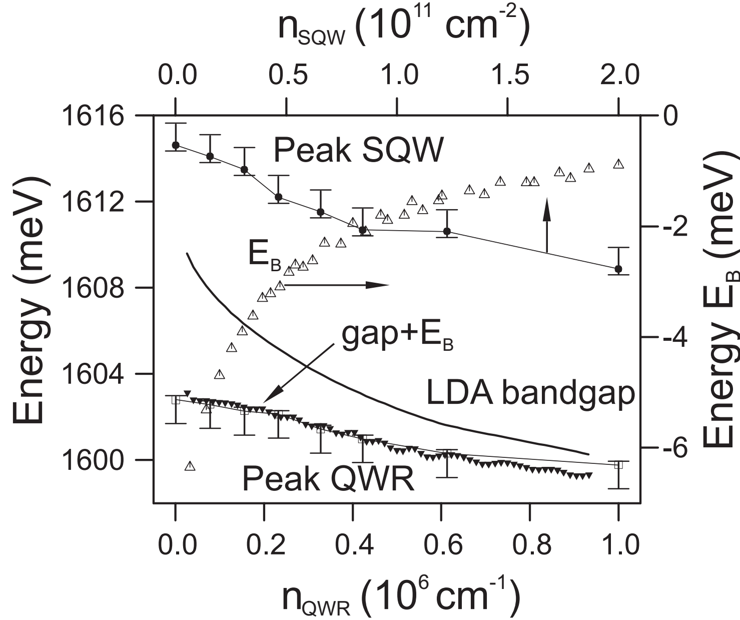

Fig. 9 Electron density dependence of the energetic peak positions of the QWRs (squares) and the SQW (dots, upper density scale), obtained by a simple line shape fit. Error bars indicate the uncertainty in determining the peak positions. The calculated LDA band gap (heavy line) and the exciton binding energy E_B (hollow triangles, right scale) combine to produce the corrected gap (solid inverted triangles) which fit the data remarkably well. Note an overall offset is arbitrary due to the choice of the bulk band gap. After [46].

4 Quantum dots

The three step growth procedure for the fabrication of T-shaped QDs is outlined below. The resulting sample structure after growth of QW layers along three orthogonal directions is shown in Fig. 10(a). The two different QD structures investigated here are sketched in Fig. 10(b) and (c). The QD superlattice structure of Fig. 10(b) consists of a 22-period GaAs/$Al_{0.35}Ga_{0.65}As$ multiple QW (MQW_1) structure with well and barrier thicknesses of 7 and 30 nm, respectively, which was two times *in situ* cleaved along the [110] and [$\bar{1}$10] cleavage planes and subsequently overgrown with two 7 nm wide GaAs single QWs (QW_2, QW_3) and $Al_{0.35}Ga_{0.65}As$ barriers. As can be seen in Fig. 10(a) three types of QWRs (QWR_{12}, QWR_{13}, QWR_{23}), resulting from intersections of MQW_1 with QW_2, MQW_1 with QW_3 and QW_2 with QW_3 form. At a length of about 800 nm 22 equally spaced and nominally identical QDs, each of which is constituted by the junction of three QWs, are located along QWR_{23}. In order to study the transition from an isolated QD (“artificial atom”) to a system of two QDs with adjustable coupling strength (“artificial molecule”) the QD structure of Fig. 10(c) has been prepared. The layer sequence of the first growth step consists in this case of a single QW followed by three pairs of QWs. The barriers separating adjacent QWs and also QDs are d = 15 nm, 30 nm and 60 nm. The spatial distance between the QDs adjusts the coupling strength of the zero-dimensional QD levels. The center-to-center distance from the single QD to the first and the following coupled QDs was chosen to be 800 nm. Further details of the two sample structures are given in Refs. [22, 23].

© 2004 WILEY-VCH Verlag GmbH & Co. KGaA, Weinheim

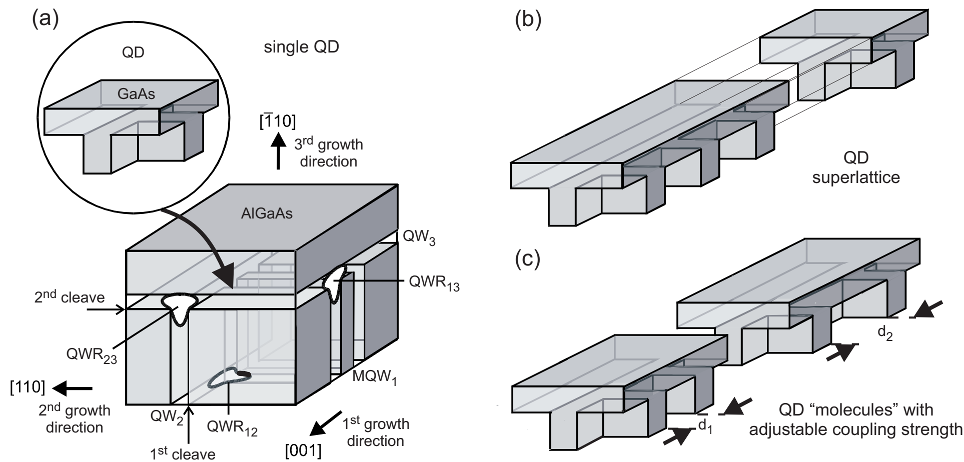

Fig. 10 (a) Schematic illustration of the QD structure (not to scale) obtained after three growth steps separated by two *in situ* cleavages. The junction of three QWs and QWRs, at which a QD forms, is shown in the magnified part of the figure. The T-shaped contours are lines of constant probability for electrons confined in the QWRs. The two sample structures investigated here consist of a QD superlattice (b) and a series of three coupled QDs with different coupling strengths as well as an individual QD (c). After [54].

The CEO QD samples were investigated using micro-photoluminescence (μPL) and μPL excitation (μPLE) spectroscopy combining high spatial and spectral resolution. Excitation was performed by means of a tunable dye laser which was focused through a microscope objective lens (numerical aperture NA = 0.75) onto the sample. The power density was kept below 50 W/cm^2. Under such conditions less than one exciton at a time is expected to be in the QDs. The samples were mounted on the cold-finger of a He cryostat and studied at nominally 5 K. The emitted light was collected by the same objective lens and directed to a confocal imaging system, which defined a nearly diffraction limited detection range of about 800 nm. Finally, the PL signal was dispersed using a triple grating Raman spectrometer (spectral resolution $\approx$ 40 μeV) and detected with a liquid nitrogen cooled charge-coupled device camera. In spite of diffraction limitation, spectroscopy of single QDs is possible using conventional optical microscopy since the CEO method allows the fabrication of QD structures with adjustable QD separations larger than the spatial resolution of the instrument. This is the case for the sample, designed to monitor subsequent phases in the formation of artificial molecules out of artificial atoms, in which all relevant QD objects, i.e. the single QD and the three coupled QD systems, can be probed individually.

We used luminescence spectroscopy with high spatial resolution (μPL) as developped by Brunner *et al.* [55, 56] to study the complicated three-dimensional structures. Figure 11 shows typical μPL spectra of the two samples recorded from the (001) and ($\bar{1}$10) surfaces as indicated in the inset. The spectrum of the superlattice QD sample (lower curve) was taken at a position in the vicinity of the QDs. As a result of the excitation geometry given in the inset of Fig. 11 all 22 QDs are excited simultaneously and contribute to the signal in the spectral range of 1560-1563 meV. It should be noted at this point that due to the large excitation area, which is unavoidable in diffraction limited spectroscopy, and exciton diffusion over a length of about 0.5 μm [50], the carriers, most of which are generated in the QW regions, recombine in the QDs, QWRs, and QWs. The relatively strong response from the QDs in spite of their extremely small volume results from efficient collection of excitons from the adjacent QWR and QW regions. Comparison with spectra taken at positions excluding excitation of the dots or wires identifies the PL response observed at 1589 meV and in the range of 1570-1580 meV as emission of MQW_1 and the two wells QW_2/QW_3. The PL energies of QW_2 and QW_3 of 1574 meV and 1576 meV determined independently in this way almost coincide, but are, as a result of the large heavy hole mass for <110> type confinement directions, well below the

© 2004 WILEY-VCH Verlag GmbH & Co. KGaA, Weinheim

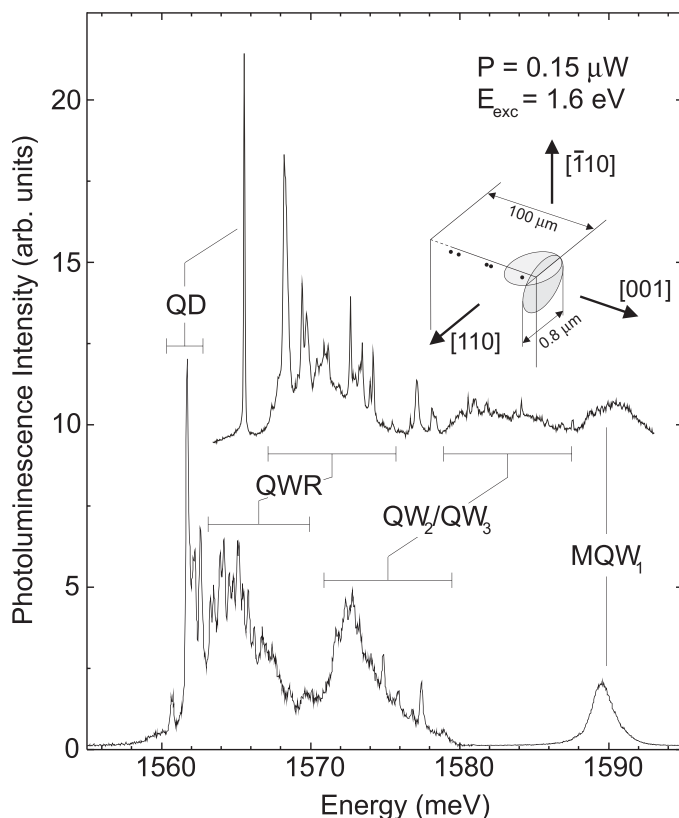

Fig. 11 μPL spectra of the samples containing the 22-period QD superlattice (lower curve) and the individual and coupled QDs (upper curve). The spectra were obtained by excitation and detection from the (001) (lower curve) and $(\bar{1}10)$ sample surfaces (upper curve), respectively, as indicated by the shaded circles in the inset (not to scale) which also schematically depicts the positions of the QDs (black dots). The two spectra are vertically offset against each other for clarity. After [54].

MQW_1 response. Emission of the three types of QWRs present in the QD structure is detected around 1565 meV. Again, the PL maxima of QWR_{12} and QWR_{13}, determined by moving the detection window away from the QD region coincide within about 1 meV. With the high spatial resolution used for these experiments we find that the QWR PL and partly that of QW_2 and QW_3 starts to decompose into sharp lines as a result of exciton localization. This effect becomes even more pronounced in the μPL spectrum of the second sample which has been taken at a position where only one QD can contribute to the signal (upper curve). Consequently, the number of localized 1D states within the excitation and collection volume is also reduced substantially and individual sharp lines start to emerge from the broad QWR background. The QD response, however, is in this case characterized by a single sharp line at an energy of 1565.9 meV, which indicates that the corresponding 0D exciton ground state is ≈ 5 meV deep with respect to the 1D QWR exciton states centered around an energy of 1571 meV. This value agrees well with the theoretical prediction for our QD structure of 6 meV [24]. Comparison of the two spectra in Fig. 11 also reveals that all PL transitions associated with the QDs, QWRs, and QW_2/QW_3 appear at lower energies in the QD superlattice sample. This is a result of slightly larger widths of QW_2 and QW_3 in this sample. However, the unambiguous assignment of the peaks to the different low-dimensional structures in Fig. 11 follows from a detailed three-dimensional μPL mapping which is presented in extracts below.

© 2004 WILEY-VCH Verlag GmbH & Co. KGaA, Weinheim

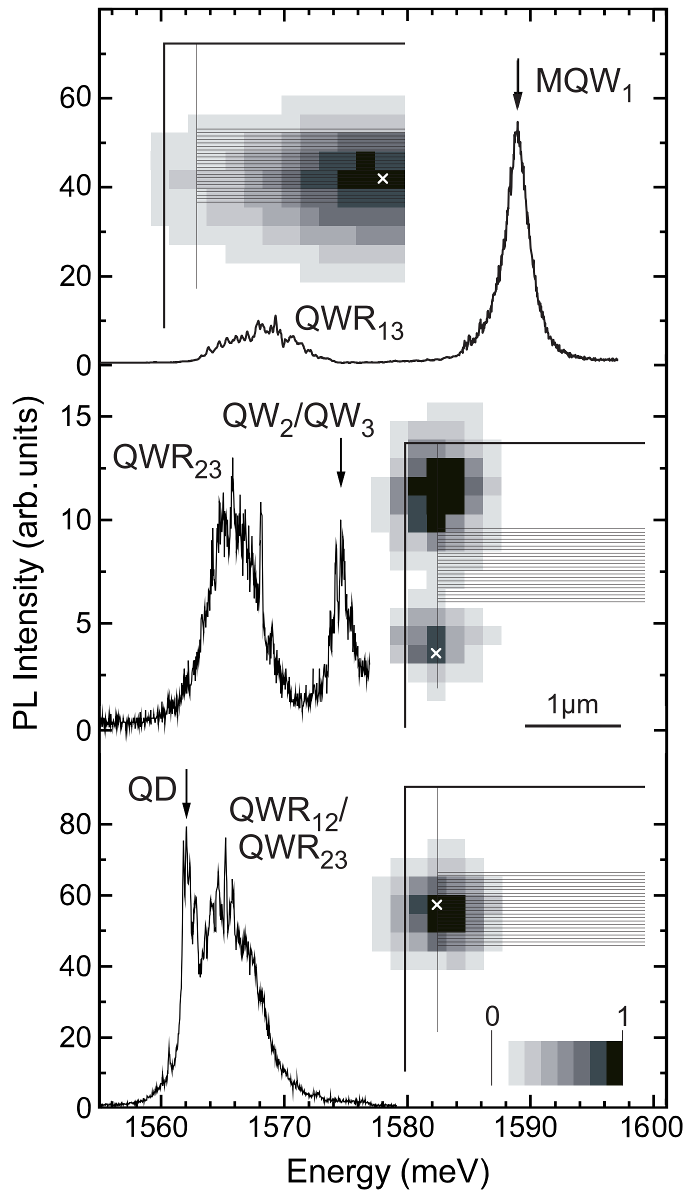

Fig. 12 μPL spectra (E_{exc} = 1.6 eV, P = 0.15 µW) and gray scale intensity plots recorded from the ($\bar{1}10$) surface of the QD superlattice sample. The positions on the sample where the spectra were taken are indicated by the white crosses in the gray scale images which are superimposed on a schematic view of the sample. The arrows define the spectral position of the corresponding gray scale plot. After [54].

4.1 Quantum dot superlattice

Figure 12 shows μPL spectra taken at different positions from the ($\bar{1}10$) surface of the QD superlattice sample together with gray scale intensity plots (pixel size 200×200 nm^2) at selected PL energies. For the position chosen in the upper panel of this figure, marked by a white cross in the gray scale image, emission from MQW_1 and QWR_{13} can be detected. The gray scale intensity plot recorded with the detection system kept fixed at the MQW_1 PL line, indicated by an arrow in the spectrum, clearly reveals quenching of the

© 2004 WILEY-VCH Verlag GmbH & Co. KGaA, Weinheim

MQW emission in the vicinity of the QDs due to exciton diffusion into wires and dots. The fact that the MQW_1 PL signal is not accordingly suppressed at positions away from the QDs but still on top of QWR_{13} is a result of the finite excitation and collection depth of our probe which exceeds the exciton diffusion length. In accordance with the detection position used for the spectrum displayed in the middle panel of Fig. 12, only signals originating from recombination within the two single QWs (QW_2, QW_3) and the single wire (QWR_{23}) which is formed by these two wells can be detected. Again, bleaching of the QW emission in the vicinity of the multiple QWRs and QDs is observed, as can be seen in the corresponding gray scale plot. Exclusively at the intersection of the wells and wires, i.e. on top of the QD array, the characteristic sharp peaks, interpreted before as PL originating from the QDs, emerge (lower panel of Fig. 12). Although the relative intensities of these peaks have changed with respect to the spectrum shown in Fig. 11 (lower PL curve), their energetic positions exactly coincide. The intensity decrease of the QD emission is limited in all directions by the experimental resolution, as demonstrated by the gray scale image taken at one of the sharp resonances. Similar intensity distributions are recorded for the other sharp peaks. They are, however, along the extension of the QD array slightly offset against each other [22]. This implies that the different QD resonances can be attributed to exciton recombination in individual spatially separated QDs of the array. The energy variations might be explained by slight differences in the widths of the participating QWs at the dot positions.

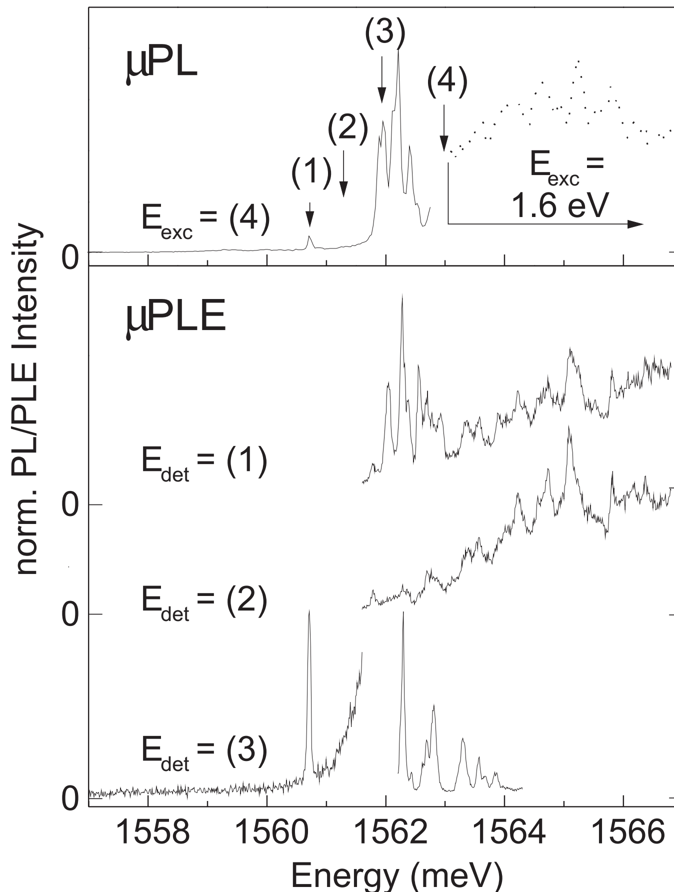

Fig. 13 Microscopic PL and PLE spectra (P = 0.4 μW) taken from the ($\bar{1}10$) surface of the QD superlattice sample at a position centered on top of the QD array. The arrows mark the energetic positions used for excitation (μPL) or detection (μPLE). After [54].

© 2004 WILEY-VCH Verlag GmbH & Co. KGaA, Weinheim

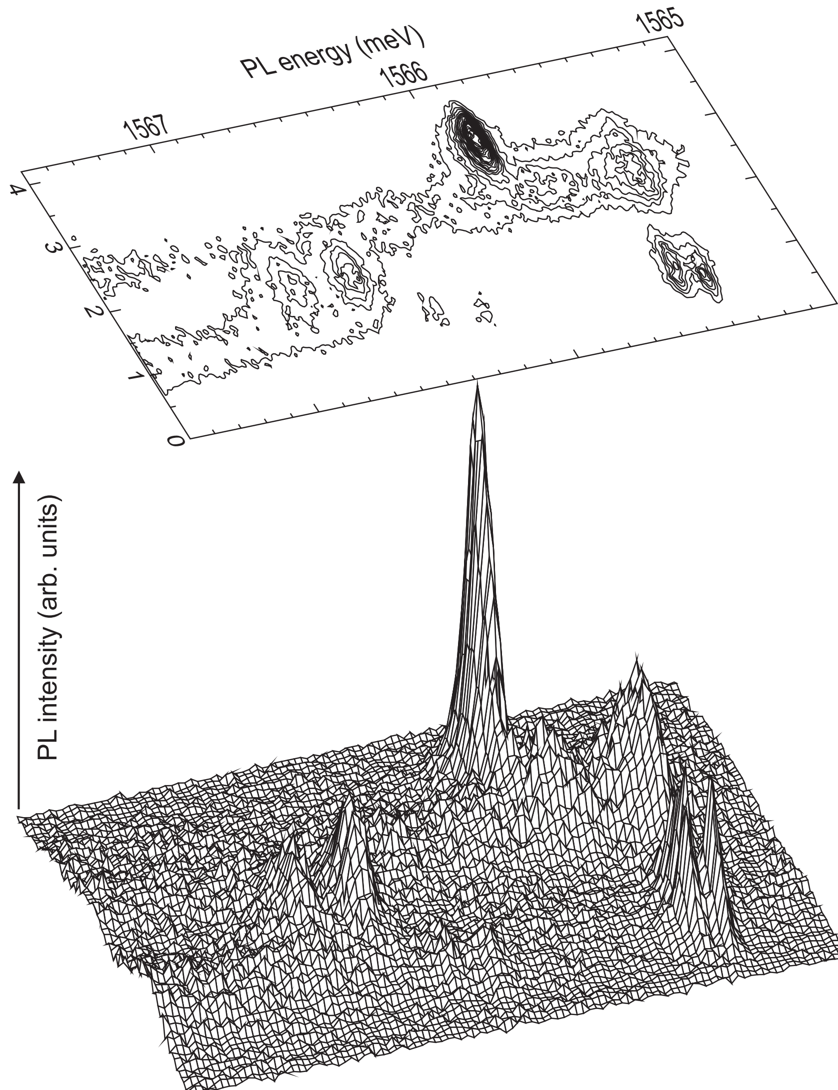

Fig. 14 Spectral image resulting from a high-resolution μPL linescan (E_{exc} = 1588 meV) along QWR_{23}, which connects the single QD with the three different coupled QDs, taken from the $(\bar{1}10)$ sample surface (lower panel). The contour lines in the upper panel of this figure represent regions of constant PL intensity of 10%, 15%, 20%,..., 95% of the maximal intensity. After [54].

Near resonant μPL and μPLE spectra of this sample are collected in Fig. 13. When the excitation is tuned to the energy labeled (4) in the upper panel of Fig. 13, the PL signal of the QDs is much clearer resolved and almost free of background. The μPLE spectrum displayed in the lower panel of Fig. 13 with the detection at the energy labeled (1), the lowest QD level, exhibits sharp resonances exactly at the QD PL energies. For energies above 1563 meV the line shape of the μPLE signal coincides with the QWR PL finestructure (dotted line). If the detection energy is slightly detuned with respect to the QD levels, for instance to the energy labeled (2), the sharp QD resonances are completely suppressed. In contrast, the QWR μPLE signal remains unchanged. For the lowest μPLE spectrum displayed in Fig. 13 the detection was moved to the energy labeled (3). Again, sharp resonances appear exactly at the energies of the other dot levels. Surprisingly, even for excitation energies smaller than the detection energy it is

© 2004 WILEY-VCH Verlag GmbH & Co. KGaA, Weinheim

possible to observe such a sharp resonance at the lowest dot level. The pronounced excitation of individual QDs under resonant pumping of QD states which are slightly above or below in energy and localized at spatially separated QDs has to be interpreted in terms of coupling of the 0D states. Such a coupling seems to be possible although the QDs are separated by 30 nm wide barriers, because the effective barrier height, represented by QWR_{23} is only ≈ 5 meV. This has been confirmed by a one-dimensional Kronig-Penney type superlattice calculation, that resulted in a ground state bandwidth of 1.7 meV. Assuming a temperature slightly higher than the nominal 5 K, the thermal energy of about 0.7 meV is comparable to the energy difference from the lowest to the higher QD levels. The observed anti-Stokes luminescence is then explained by thermally activated tunneling of excitons from one QD to another.

4.2 Transition from an artificial atom to a molecule

Deeper insight into the effects of quantum mechanical coupling between 0D exciton states in two QDs can be gained by a detailed analysis of the sample which contains a single QD as well as a series of pairs of QDs with different coupling strengths. Figure 14 shows the spectral image of a linescan along QWR_{23} in this sample on an enlarged energy scale. The image is dominated by the single line, which is also visible in the upper PL spectrum of Fig. 11, and which originates from excitons recombining within the single QD.

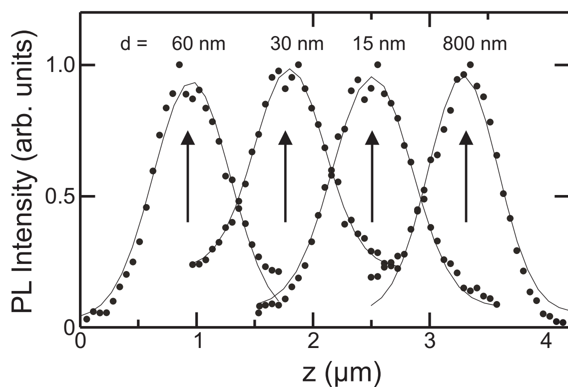

Fig. 15 Normalized PL intensities integrated over the spectral regions of maxima in Fig. 14, centered at about 1565.42 meV (d = 60 nm), 1566.63 meV (d = 30 nm), 1565.70 meV (d = 15 nm), and 1565.89 meV (d = 800 nm, single QD) and plotted as a function of the position along the linescan. The nominal positions of the different QD structures are indicated by the arrows in this plot. The solid curves are just guides to the eye. After [54].

Moving the excitation and detection window to the coupled QDs, a series of double peaks appears. The spatial positions of all peaks exactly coincide with the designed positions of our individual and coupled QDs as can be seen by the integrated PL intensity plots of Fig. 15, in which the nominal QD positions are marked by arrows. The spatial width of these peaks is comparable to that observed for the different transitions in the QD superlattice sample and is limited by the spatial resolution of the μPL setup. This clear correlation of the sharp lines with position directly proves that they originate from excitonic recombination in the CEO QDs. The energetic spread of the peaks in the range of 1 to 2 meV can be well described by monolayer thickness fluctuations in the overgrown QWs. However, the wave functions of the coupled QDs probe only a very short part of the constituting QWs with respect to the length scale of monolayer fluctuations and coupling between almost identical objects can be studied.

The appearance of two energetically distinct peaks from coupled QDs, as shown in Fig. 16(a), is clear evidence that their excitonic levels are coupled. This scenario of an exciton bound to two QDs can be compared to the synthesis of a positively charged hydrogen molecule H_2^+ from an electron and two protons, a system that can be described in the framework of elementary quantum mechanics by the formation of

© 2004 WILEY-VCH Verlag GmbH & Co. KGaA, Weinheim

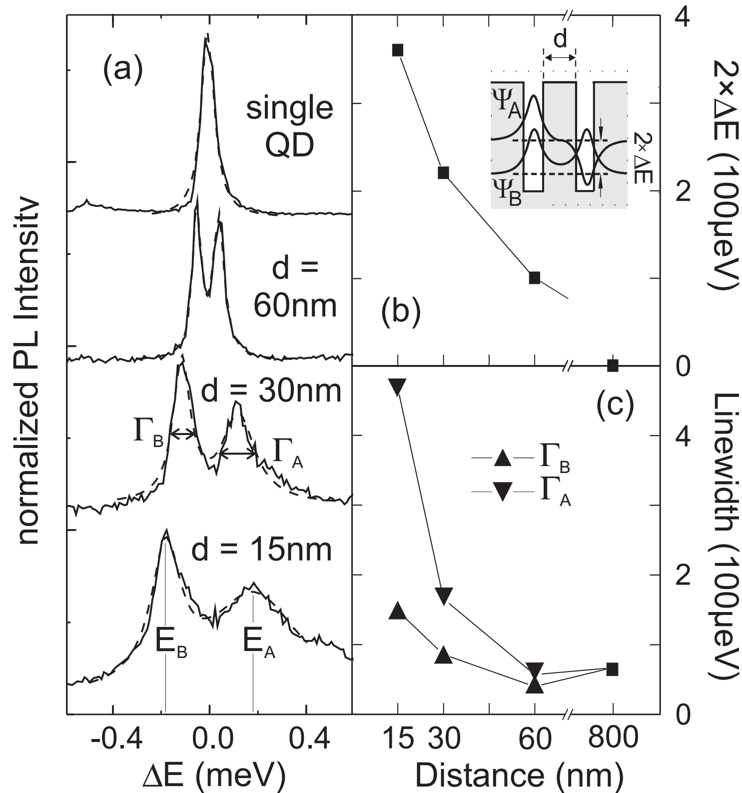

Fig. 16 (a) Selected normalized μPL spectra from the linescan of Fig. 14 of the single and the coupled QDs (at the positions marked by the arrows), plotted on a relative energy scale and offset vertically against each other for clarity, (b) energetic splitting between the bonding and antibonding levels as indicated in the inset, and (c) linewidths of the two levels as a function of the QD distance d. The solid lines in (b) and (c) are a guide for the eye. After [54].

bonding and antibonding states. The influence of coupling on the excitonic levels, on the order of 100 µeV, is, however, small compared to the binding energy of an exciton confined to a CEO QD of more than 10 meV. Therefore, the exciton is considered as one particle whose internal structure is not affected by coupling. In analogy to the two coupled electronic levels of the H_2^+ molecule, the wave function ψ of the system of two coupled excitonic 0D levels can be approximated by the sum and difference of the wave functions of individual 0D states. These wave functions, ψ_B and ψ_A, correspond to the bonding and antibonding states as visualized in the schematic drawing of the one-dimensional potential profile for excitons in the coupled system of Fig. 16(b). From first-order perturbation theory, the energy levels of the coupled system can be written as $E_{B/A} = E_0 \mp \Delta E$, where E_0 is the energy level of an individual QD and ΔE is a matrix element that describes the energetic splitting $2 \times \Delta E$ caused by coupling. Following this argument, we assign the two energetically distinct PL lines of each coupled QD to emission from bonding and antibonding energy levels, which are separated by $2 \times \Delta E$. The observed systematic dependence of the energetic splitting on the distance between the coupled dots [Fig. 16(b)] confirms this interpretation in terms of bonding and antibonding states. The enhancement of the energetic splitting with decreasing distance between the coupled QDs directly reflects the increasing coupling strength of the 0D levels.

In agreement with results obtained on naturally formed QDs [57] the spectra shown in Fig. 16(a) are well fitted with Lorentzian functions (dashed curves). This implies that the PL linewidths corresponding

© 2004 WILEY-VCH Verlag GmbH & Co. KGaA, Weinheim

to the bonding and antibonding states are life-time broadened. These linewidths increase systematically with increasing coupling strength [Fig. 16(c)]. The broadening is especially pronounced for emission from the antibonding level. This decrease of the exciton lifetime for the antibonding state with increasing level separation might be due to acoustical phonon scattering from the upper into the lower state [58]. In such a simple two-level picture one would expect a cubic dependence of the linewidth of the upper level on the energy level separation, which is also observed experimentally.

4.3 Cleaved edge overgrowth assisted self-assembled quantum dots

Our new approach to grow systems of aligned and well ordered QDs is to combine the well established self-assembled QD growth with the CEO method. In a first MBE step we have grown a number of epitaxial layers on a (001) GaAs substrate, which act as a template for QD nucleation during a subsequent second MBE growth run on the cleaved ($1\bar{1}0$) surface.

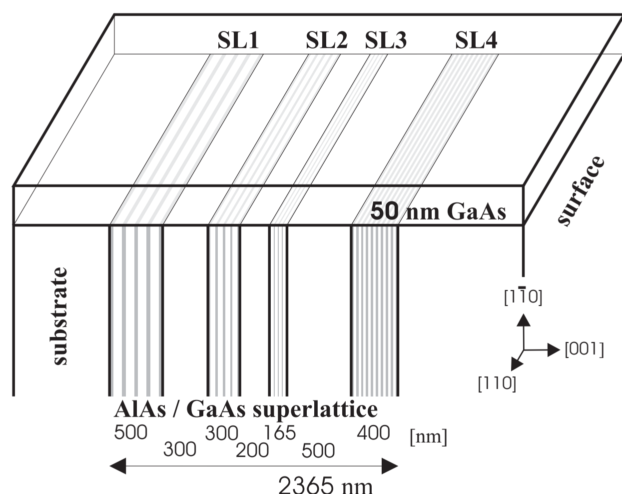

Fig. 17 Schematic of the grown layer sequence: In the first growth step the superlattices SL1-SL4 were grown on semi-insulating (001)-oriented GaAs. The InAs dot layer and a 50 nm thick capping layer were grown in a subsequent MBE run on the ($1\bar{1}0$) GaAs surface.

The sample we investigated (see Fig. 17) consists of 4 spatially separated superlattices (SL1: 5 periods of 32 nm AlAs and 68 nm GaAs; SL2: 5 periods of 20 nm AlAs and 40 nm GaAs; SL3: 5 periods of 11 nm AlAs and 22 nm GaAs; SL4: 10 periods of 20 nm AlAs and 20 nm GaAs) grown on semi-insulating (001) GaAs. Immediately after cleaving the substrate in the growth chamber we deposited 3 ML InAs on the ($1\bar{1}0$) surface. For samples which were designed for atomic force microscopy (AFM) investigations growth was stopped after this step, whilst for PL measurements the InAs layer was covered with 50 nm GaAs to bury the QD layer. Growth on the ($1\bar{1}0$) surface was performed at T_{subs} = 470°C, R_{In} = 0.01 nm/s and R_{Ga} = 0.18 nm/s.

Figure 18 shows an AFM picture of the uncapped sample. QD-like nanostructures can clearly be identified above all four superlattice regions SL1-SL4 [59]. Most surprisingly, the AFM measurements clearly indicate nucleation of QD-like nanostructures along the Al-rich regions of the ($1\bar{1}0$) growth surface. Furthermore, the typical size of the QDs reflects the thickness of the underlying AlAs layer; being largest for SL1 (32 nm AlAs), smallest for SL3 (11 nm AlAs) and comparable for SL2 and SL4 which share a common AlAs width (20 nm) but differ in the thickness of the surrounding GaAs and in the total number of periods. However the QDs grown on SL2 and SL4 appear to have slightly different sizes and also different interdot distances. We conclude, therefore, that the geometric properties of the QDs are sensitive not only to the thickness of the underlying AlAs layers but also that the surrounding GaAs plays an important role

© 2004 WILEY-VCH Verlag GmbH & Co. KGaA, Weinheim

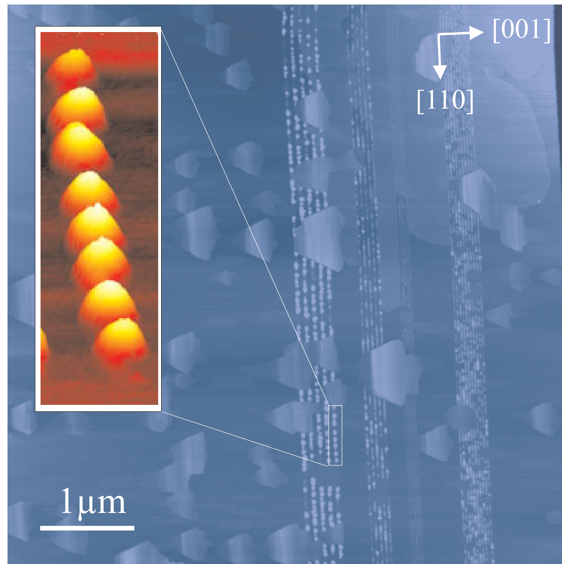

Fig. 18 Atomic force microscopy picture of the well ordered InAs QDs. The inset shows a close-up of 8 perfectly aligned QDs similar in size and shape. In the upper right corner of the picture the edge of the sample is visible.

for QD nucleation. We suggest the following mechanism leading to dot growth on the $(1\bar{1}0)$ AlAs layers: due to the higher desorption rate of In atoms on GaAs compared with AlAs and the lower In adatom mobility on Al-containing layers [60] there is an effective mass flow towards the AlAs layers. On top of these layers, the strain caused by the lattice mismatch between InAs and AlAs is reduced by the formation of a one-dimensional ordered array of QDs. The lower In adatom mobility may be the reason why strain is not reduced by dislocations as known for InAs growth on (110) oriented GaAs [61] but by nucleating in QDs. Similar results pertaining to QD growth on (110) AlAs were obtained in a recent work by Wassermann *et al.* [62]. In the AFM image (Fig. 18) one can also identify much larger triangular islands with a height of some monolayers. We attribute these islands to excess InAs, comparable to similarly formed GaAs islands on a cleaved $(1\bar{1}0)$ surface reported by Yoshita *et al.* [63], referring to a similar mechanism of adatom migration both for GaAs and InAs growth.

In order to investigate the optical properties of the QD nanostructures we performed scanning μPL spectroscopy on a subsequently grown sample. The sample was mounted in a liquid He cryostat ($T \approx 10$ K) with the QD layer facing the incident laser beam and the optics to collect PL light. To excite the QDs, we used a HeNe laser, focused on the $(1\bar{1}0)$ surface of the sample and a confocal excitation and collection geometry resulting in a maximum spatial resolution of approximately 1.5 µm. The excitation spot was then raster scanned across the sample $(1\bar{1}0)$ surface to obtain a spatially and spectrally resolved image of the optical emission characteristics. Spectra, taken at different positions along the $[00\bar{1}]$ direction (referred to as 'y-direction', see also Fig. 17) with $\Delta y = 0.2$ µm are presented in Fig. 19.

In this figure four different groups of sharp PL peaks can be seen around 1.325 eV (PL1), 1.356 eV (PL2), 1.372 eV (PL4), and 1.389 eV (PL3). By examining the spatial distribution of these luminescence peaks and correcting for the spatial resolution of 1.5 µm we deduce the positions on the $(1\bar{1}0)$ surface of the underlying luminescence centers. The positions obtained in this way and the distance between the luminescence center near the edge of the sample (PL4) and the most inner one (PL1) are in quite good agreement with the geometric properties of the superlattice substrate (see Fig. 17). This coincides with the AFM measurements (Fig. 18) and tends to confirm that larger dots, with larger confinement, are nucleated above SL1. The PL signal labeled as group PL4 arises from a location next to the edge of the sample, and

© 2004 WILEY-VCH Verlag GmbH & Co. KGaA, Weinheim

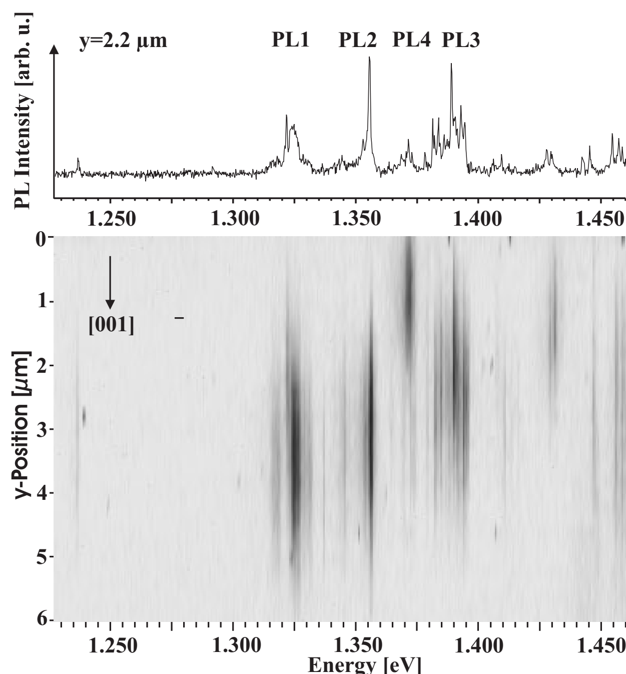

Fig. 19 μPL spectra of the InAs QDs on the $(1\bar{1}0)$ cleaved surface taken at different positions along $[00\bar{1}]$ direction. The position given is relative to the edge of the sample at y = 0.0 µm. The peaks between 1.3 eV and 1.4 eV are attributed to the buried InAs QD layer. In the upper part, the spectrum taken at the position y = 2.2 µm is presented for comparison.

the signal of group PL3 is the following one in $[00\bar{1}]$ direction towards bulk material. Furthermore, the peaks of group PL3 show higher PL energy and consist of more than only one sharp line compared to PL in group PL4. Based on these observations we suggest that the PL signals of group PL4 belong to somewhat larger QDs grown on SL4, whilst the blueshifted PL signals of group PL3 belong to smaller QDs nucleated above SL3. This assumption is also in qualitative agreement with the thickness of the AlAs layers in the respective superlattices (SL3: 11 nm, SL4: 20 nm). The smaller QDs on SL3 are likely to be less uniform and they may have a lower density, thus explaining the existence of more pronounced sharp lines in the spectrum. According to the energies of the PL signals in group PL1 and PL2, we suggest that PL signals of group PL1 belong to the largest QDs grown on SL1 and that the PL signals of group PL2 belong to QDs nucleated above SL2. Additionally, the locations of the maximum intensities of the relevant peaks in these two groups are in very good agreement with the respective positions of SL1 and SL2 inside the sample. PL spectra recorded from positions further from the edge of the sample showed characteristically broader luminescence arising from the GaAs substrate but no sharp-line emission in the spectral window below 1.45 eV. This observation strongly supports our identification of the sharp-line emission as arising from self-assembled QDs which are spatially ordered into one-dimensional arrays along the AlAs regions of the $(1\bar{1}0)$ surface.

In order to further substantiate our assumption that the sharp-emission lines are due to laterally ordered self assembled QDs, we performed power dependent PL measurements at a specific position of SL1. The result of these measurements are summarized in Fig. 20. At low excitation power, just a single emission line at 1.308 eV is observed. The linear power dependence of this feature identifies it as arising from a single exciton. In addition, this line is an emission doublet, possibly due to elongation of the QDs along the AlAs layer and the resulting electron-hole exchange interaction in the QD with reduced symmetry

© 2004 WILEY-VCH Verlag GmbH & Co. KGaA, Weinheim

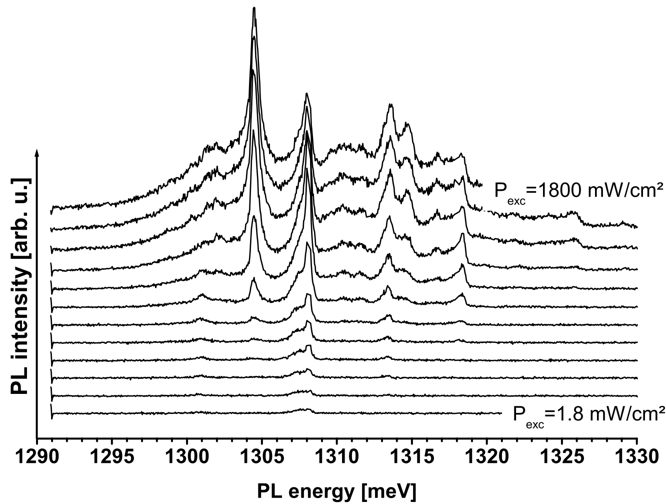

Fig. 20 μPL spectra of a single InAs QD on the $(1\bar{1}0)$ cleaved surface as a function of excitation power. For clarity, subsequent spectra are offset vertically.

[64]. Upon increasing the excitation power density, several sharp lines at lower (1.3044 eV) and higher (1.3135 eV, 1.3148 eV, 1.3166 eV, and 1.3182 eV) energies emerge. In particular, the intensity of the emission line at 1.3044 eV increases quadratically with excitation power density and dominates the spectra for the highest excitation densities investigated. This characteristic behavior identifies this peak as arising from bi-exciton recombination in the dot [55]. The other lines probably arise from more complicated exciton configurations including charged excitons [65].

5 Purely strain induced single quantum wires

In order to fully exploit the one-dimensional character of QWR devices, the difference between the smaller transition energy of the two involved QWs and that of the QWR has to be large. For this energy difference or confinement energy, maximal values of 38 meV [66] and 54 meV [28] were reported. Strained systems are considered to have the capability of further enhancing the confinement energy. Even before the realization of the first T-shaped QWRs [67], Gershoni *et al.* presented a concept of strain induced confinement [68]. In more recent works, values of 34 meV [69] and 41 meV [70] were measured for strained samples with two QWs forming the T-shaped junction.

In this section we present a structure where strong confinement is achieved purely by lateral strain variation within a single QW. Calculations of Grundmann *et al.* predict confinement energies of up to 90 meV for such systems [71]. In conventional T-shaped structures, the QWRs are formed by the spreading of the wave function into the two adjacent wells as already explained in section 3. Here, an $In_{0.16}Al_{0.84}As$ stressor layer replaces the QW along the [001] direction (see Fig. 21). This concept differs from that in Ref. [68] where an $In_{0.063}Ga_{0.937}As$/GaAs superlattice serving as stressor material made it necessary to grow an $Al_{0.3}Ga_{0.7}As$ barrier on the cleaved edge before depositing the GaAs QW. The advantage of $In_{0.16}Al_{0.84}As$ is that it acts as a barrier for both electrons and holes in the overgrown QW rejecting the carriers from the strained layer. This is why the (110) QW can be grown directly on the cleaved edge, thus permitting a strong strain modulation. The QWRs form within the QW exactly where the material is subject to tensile strain due to the underlying $In_{0.16}Al_{0.84}As$ layers, although these films act as barriers. We study the optical properties of these GaAs/$In_{0.16}Al_{0.84}As$ QWRs and find a systematic dependence of the confinement on the widths of the stressor layers and overgrown layers. High confinement energies of

© 2004 WILEY-VCH Verlag GmbH & Co. KGaA, Weinheim

up to 51.5 meV were obtained, where a 12 nm $In_{0.16}Al_{0.84}As$ layer has been overgrown by a 10 nm GaAs QW.

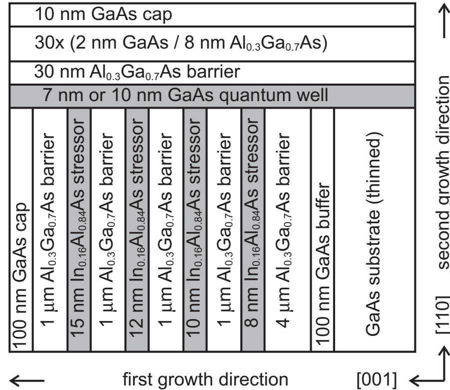

Fig. 21 Cross-sectional representation of the purely strain induced QWR sample. Each QWR is located in the QW and forms exclusively by the strain field from the $In_{0.16}Al_{0.84}As$ stressor layer. For sample A and B this QW has a thickness of 7 nm and 10 nm, respectively.

The detailed design, which follows closely the suggestion of Regelman *et al.* [72], is given in Fig. 21. An elaborate investigation of such a structure by means of grazing incidence x-ray diffraction is reported elsewhere [73]. In the first growth step, four stressor layers separated by 1 µm wide $Al_{0.3}Ga_{0.7}As$ barriers were grown. This design enables us to spatially resolve individual QWRs. In each sample, the stressor layers have widths of 8, 10, 12, and 15 nm. However, the thickness of the overgrown GaAs QW in sample A and B is 7 and 10 nm, respectively. The signals of the QWRs and QWs were again detected by a μPL setup. The incident laser beam was perpendicular to the plane of projection in Fig. 21 and had a full width at half maximum (FWHM) spot size of roughly 800 nm exciting the sample with 1.0 µW. The assignment of the peaks to the various quantum structures was carried out by scanning the PL intensity spatially with a step width of 100 nm in both the [001] and the [110] direction. All experiments were performed at a temperature of 5 K.

Corresponding to the five quantum structures in sample A, four PL signals from the QWRs and one peak from the overgrown QW were detected and are shown in Fig. 22. The PL light from the QW exhibits a double peak structure and is centered around 1563 meV. Temperature dependent measurements confirmed that the low energy shoulder is due to localized states. The FWHM linewidth of this signal, which was obtained at the lateral position of the 4 µm wide $Al_{0.3}Ga_{0.7}As$ barrier, i.e. away from QWRs, is 13 meV. The absolute PL intensity of this QW peak shows pronounced minima where the $In_{0.16}Al_{0.84}As$ stressor layers are located. At exactly these positions, where the QW emission is suppressed, four signals with different photon energies can be detected, each of them locally confined. This is shown in the inset of Fig. 22, where the intensity distributions at the junction of the 8 nm stressor layer with the 7 nm wide GaAs QW (QWR1) are depicted. The white lines mark exactly the position where the T-shaped intersection is expected, since both the wire to wire and the wire to sample edge distance are known due to the MBE controlled layer widths. In this way, the individual QWRs can be identified unambiguously. Clearly, the QWR emission coincides locally with a minimum in the PL intensity of the QW. The QWR PL peak (QWR1) is centered at 1544 meV, having a FWHM linewidth of 8 meV. Analogously, localized PL emission from QWR2, QWR3, and QWR4 can be detected at the positions of the 10, 12, and 15 nm wide $In_{0.16}Al_{0.84}As$ layers. These peaks are centered at 1535, 1526, and 1523 meV and exhibit FWHM linewidths of 7, 7, and 9 meV, respectively. It is remarkable that the QWR intensities are comparable with the QW emission, although their cross-sectional areas differ by roughly two orders of magnitude. This points toward strong charge carrier or exciton diffusion within the area of excitation as observed in

© 2004 WILEY-VCH Verlag GmbH & Co. KGaA, Weinheim

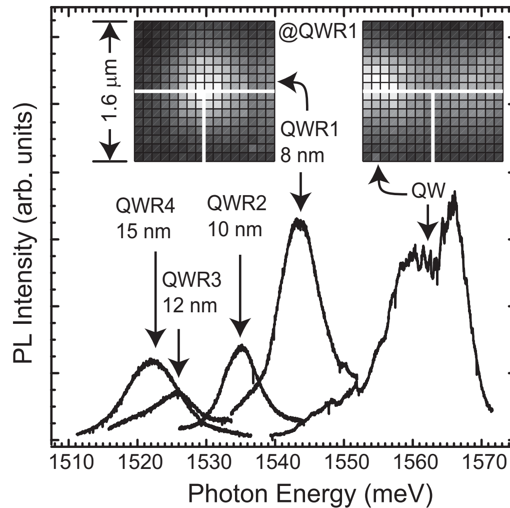

Fig. 22 PL signals of four individual T-shaped QWRs and of the reference GaAs QW of sample A. The inset shows the spatial PL intensity distributions of QWR1 and the GaAs QW at the position of QWR1 (white lines mark the T-shaped intersection). The intensity of QWR1 is high (bright), where the QW intensity shows a minimum (dark).

T-shaped QWRs [50] and directly reveals the absence of dislocations or other sources of non-radiative recombination centers in the vicinity of the purely strain induced QWRs.

w_{InAlAs} (nm)	Sample A w_{GaAs} = 7 nm E_c (meV)	Sample B w_{GaAs} = 10 nm E_c (meV)
8	19	22
10	28	33
12	37	41
15	40	-

Table 1 Experimentally determined confinement energies E_c as a function of the layer widths w_{GaAs} and w_{InAlAs} of the overgrown GaAs QW and the $In_{0.16}Al_{0.84}As$ stressor layers.

Analogous measurements were repeated for sample B, where the layer width w_{GaAs} of the overgrown GaAs QW is 10 nm. However, only three of the expected four signals could be detected. This might be due to dislocations which are introduced when the critical thickness is reached during the growth process. This is supported by the fact that it is the emission of the QWR with the thickest stressor layer which cannot be observed. Another possible reason are cleavage problems. They are confirmed by AFM surveys of the $(\bar{1}10)$ surface obtained after a second *ex situ* cleavage, which revealed that the strained layers are often accompanied by parallel steps with heights up to 70 nm, especially for large indium contents. The values of the confinement energy of these QWRs, however, systematically increase with the width w_{InAlAs} of the stressor layer as documented in Table 1. Additionally, the confinement in sample B is larger than in sample A. This is in agreement with Ref. [71], where the calculated confinement energy rises when either w_{GaAs} is changed from 5 to 10 nm for fixed w_{InAlAs} = 10 nm or w_{InAlAs} is changed from 10 to 15 nm for fixed w_{GaAs} = 10 nm.

© 2004 WILEY-VCH Verlag GmbH & Co. KGaA, Weinheim

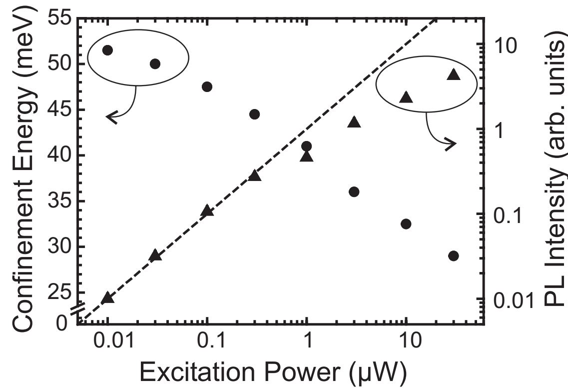

Fig. 23 Confinement energy E_c and PL intenisity of the strained QWR at the T-shaped intersection of the 12 nm wide $In_{0.16}Al_{0.84}As$ stressor layer and the 10 nm wide overgrown GaAs QW in sample B as a function of the excitation power.

We have also carried out excitation power dependent measurements. The results are shown in Fig. 23, where the confinement energy at the intersection of the 12 nm wide $In_{0.16}Al_{0.84}As$ layer and the 10 nm wide overgrown QW (sample B) reaches values of up to 51.5 meV. The observed blueshift with increasing excitation power is most probably the consequence of the screening of the strain induced electric fields. The absolute PL peak intensity increases linearly with the incident power for weak excitation and starts saturating at approximately 1 µW as can be seen in Fig. 23. Even for the lowest excitation power the line shapes of the QWR peaks remain smooth (see Fig. 24), while in unstrained T-shaped QWRs characteristic series of narrow peaks are observed [51, 74], originating from exciton localization due to heterointerface roughness. These monolayer thickness fluctuations can be reduced by annealing the surface during an interrupt of the growth process [63]. Since the investigated samples were grown without annealing, the smoothness of the QWR peaks comes unexpectedly and can only be interpreted as sub-exciton diameter scale interface roughness fluctuations along the wire. Despite the high confinement energy, the QWR emission cannot be observed at room temperature. The only explanation for this PL intensity drop is a strong increase of the non-radiative recombination rate at higher temperatures, which might be correlated to the peculiar conditions for GaAs (110) growth [19]. We would like to note here that the necessary suppression of the non-radiative recombination could be achieved by the recently introduced annealing technique [63].

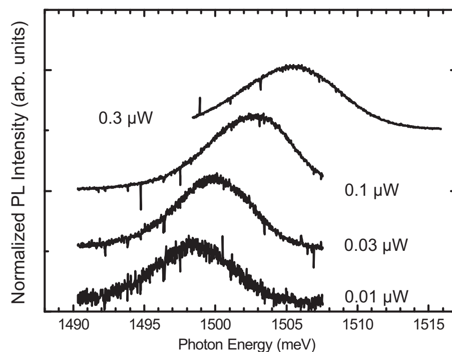

Fig. 24 The μPL spectra corresponding to the data points for low excitation powers given in Fig. 23 exhibit smooth line shapes.

© 2004 WILEY-VCH Verlag GmbH & Co. KGaA, Weinheim

In order to optimize the sample parameters, numerical simulation have been carried out. In Fig. 25 the relative hydrostatic strain e_{hyd} is plotted gray scale coded as a function of the position on a 60 × 60 nm^2 large region. The depicted area represents only a small fraction of the overall simulated region and is oriented in accordance with Fig. 21. Whereas the 15 nm wide $In_{0.16}Al_{0.84}As$ layer is compressively strained, the overgrown 10 nm wide GaAs QW is almost unstrained, except for the region directly above the stressor layer. Here, it can be clearly seen that QWRs can form in a locally confined area, because the present tensile strain field alters the band structure in a way that the band gap is lowered.

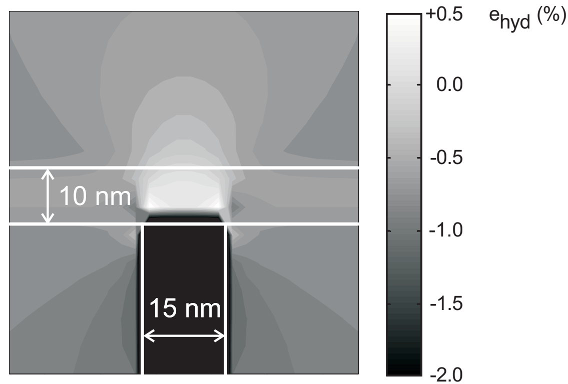

Fig. 25 Relative hydrostatic strain e_{hyd} as a function of the position on a 60 × 60 nm^2 large region. Above the 15 nm wide $In_{0.16}Al_{0.84}As$ layer the 10 nm wide GaAs QW is subject to tensile strain. (Orientation similar to Fig. 21.)

6 Conclusions

Cleaved edge overgrowth has proven to be a powerful technique for the fabrication of QWRs and QDs with applications in optics and, not subject of this article, transport. The T-geometry QWRs represent a model system for other 1D structures with typical dimensions comparable to the exciton Bohr radius. For these structures excitonic effects become increasingly important and strongly influence the optical properties. We showed that the emission of T-QWR lasers is subject to a strong magnetic field dependence. For magnetic fields oriented perpendicular to the QWR axis a standard rate equation model incorporating the excitonic nature of the transitions explained the observed behavior. The band gap renormalization of modulation doped QWRs is weaker than that of the QW. Single and multiple QDs were identified by spatially resolved PL measurements. The coupling between "artificial atoms" has been presented and is in full agreement with the theoretical expectations. In this way, T-shaped QDs allow the experimental investigation of a variety of quantum mechanics textbook examples previously inaccessible by other means. Long-range ordered arrays of self-assembled QDs have been grown successfully on cleaved (110) GaAs. Both AFM and PL experiments show that precise control of size and order is possible due to the underlying AlAs/GaAs superlattices. The fabricated QDs show excellent optical properties and have a high potential for well defined coupled systems. The introduction of strain adds another degree of freedom for designing CEO structures. The concept of enhancing the confinement energy by using stressor layers has been demonstrated and should be transferable to QD systems, which are currently of interest in the context of solid state quantum computing.

Acknowledgements This work summarizes the major results obtained within TP A10 of Sonderforschungsbereich 348 over the past 9 years. The financial support by the DFG is gratefully acknowledged.

© 2004 WILEY-VCH Verlag GmbH & Co. KGaA, Weinheim

References

[1] C. Weisbuch and B. Vinter, Quantum Semiconductor Structures (Academic Press, San Diego, 1991), pp. 191–193.
[2] E. Kapon, D. M. Hwang, and R. Bhat, Phys. Rev. Lett. **63**, 430 (1989).
[3] M. Tsuchiya, J. M. Gaines, R. H. Yan, R. J. Simes, P. O. Holtz, L. A. Coldren, and P. M. Petroff, Phys. Rev. Lett. **62**, 466 (1989).
[4] R. Nötzel, N. N. Ledentsov, L. Däweritz, M. Hohenstein, and K. Ploog, Phys. Rev. Lett. **67**, 3812 (1991).
[5] S. Tsukamoto, Y. Nagamune, M. Nishioka, and Y. Arakawa, Appl. Phys. Lett. **63**, 355 (1993).
[6] K. Brunner, U. Bockelmann, G. Abstreiter, M. Walther, G. Böhm, G., Tränkle, and G. Weimann, Phys. Rev. Lett. **69**, 3216 (1992).
[7] F. E. Prins, G. Lehr, M. Burkard, H. Schweizer, M. H. Pillkuhn, and G. W. Smith, Appl. Phys. Lett. **62**, 1365 (1993).
[8] A. Hartmann, L. Loubies, F. Reinhardt, and E. Kapon, Appl. Phys. Lett. **71**, 1314 (1997).
[9] A. Hartmann, Y. Ducommun, L. Loubies, K. Leifer, and E. Kapon, Appl. Phys. Lett. **73**, 2322 (1998).
[10] P. Ballet, J. B. Smathers, H. Yang, C. L. Workman, and G. J. Salamo, J. Appl. Phys. **90**, 481 (2001).
[11] R. Nötzel and K. H. Ploog, J. Cryst. Growth **227–228**, 8 (2001).
[12] H. J. Kim, Y. J. Park, Y. M. Park, E. K. Kim, and T. W. Kim, Appl. Phys. Lett. **78**, 3253 (2001).
[13] R. Leon, S. Chaparro, S. R. Johnson, C. Navarro, X. Jin, Y. H. Zhang, J. Siegert, S. Marcinkevičius, X. Z. Liao, and J. Zou, J. Appl. Phys. **91**, 5826 (2002).
[14] B. D. Gerardot, G. Subramanian, S. Minvielle, H. Lee, J. A. Johnson, W. V. Schoenfeld, D. Pine, J. S. Speck, and P. M. Petroff, J. Cryst. Growth **236**, 647 (2002).
[15] R. Songmuang, S. Kiravittaya, and O. G. Schmidt, Appl. Phys. Lett. **82**, 2892 (2003).
[16] T. Ogawa and T. Takahara, Phys. Rev. B **44**, 8138 (1991).
[17] A. L. Ivanov and H. Haug, Phys. Rev. Lett. **71**, 3182 (1993).
[18] W. Wegscheider, L. N. Pfeiffer, A. Pinczuk, K. W. West, M. M. Dignam, R. Hull, and R. E. Leibenguth, J. Cryst. Growth **150**, 285 (1995).
[19] L. Pfeiffer, K. W. West, H. L. Stormer, J. P. Eisenstein, K. W. Baldwin, D. Gershoni, and J. Spector, Appl. Phys. Lett. **56**, 1697 (1990).
[20] W. Wegscheider, L. N. Pfeiffer, and K. W. West, in: Festkörperprobleme/Advances in Solid State Physics, Vol. 35, edited by R. Helbig (Vieweg, Wiesbaden, 1996), p. 155.
[21] Y.-C. Chang, L. L. Chang, and L. Esaki, Appl. Phys. Lett. **47**, 1324 (1985).
[22] W. Wegscheider, G. Schedelbeck, G. Abstreiter, M. Rother, and M. Bichler, Phys. Rev. Lett. **79**, 1917 (1997).
[23] G. Schedelbeck, W. Wegscheider, M. Bichler, and G. Abstreiter, Science **278**, 1792 (1997).
[24] M. Grundmann and D. Bimberg, Phys. Rev. B **55**, 4054 (1997).
[25] G. Bastard and J. Y. Marzin, Solid State Commun. **91**, 39 (1994).
[26] A. A. Kiselev and U. Rössler, Semicond. Sci. Technol. **11**, 203 (1996).
[27] L. Pfeiffer, H. Baranger, D. Gershoni, K. Smith, and W. Wegscheider, in: Low Dimensional Structures Prepared by Epitaxial Growth or Regrowth on Patterned Substrates, edited by K. Eberl, P. M. Petroff, and P. Demeester (Kluwer Academic, Dordrecht, 1995), pp. 93–100.
[28] W. Langbein, H. Gislason, and J. M. Hvam, Phys. Rev. B **54**, 14595 (1996).
[29] A. Löffler, D. Brinkmann, and G. Fishman, in: Semiconductor Heteroepitaxy. Growth, Characterization and Device Applications, edited by B. Gil and R.-L. Aulombard (World Scientific, Singapore, 1995), p. 375.
[30] G. W. Bryant, P. S. Julienne, and Y. B. Band, unpublished.
[31] S. Glutsch, F. Bechstedt, W. Wegscheider, and G. Schedelbeck, Phys. Rev. B **56**, 4108 (1997).
[32] Y. Arakawa and H. Sakaki, Appl. Phys. Lett. **40**, 939 (1982).
[33] Y. Arakawa, H. Sakaki, M. Nishioka, H. Okamoto, and N. Miura, Jpn. J. Appl. Phys. **22**, L804 (1983).
[34] T. T. J. M. Berendschot, H. A. J. M., Reinen, H. J. A. Bluyssen, C. Harder, and H. P. Meier, Appl. Phys. Lett. **54**, 1827 (1989).
[35] Y. Arakawa, K. Vahala, A. Yariv, and K. Lau, Appl. Phys. Lett. **47**, 1142 (1985).
[36] Y. Arakawa, K. Vahala, A. Yariv, and K. Lau, Appl. Phys. Lett. **48**, 384 (1986).
[37] K. Vahala, Y. Arakawa, and A. Yariv, Appl. Phys. Lett. **50**, 365 (1987).
[38] W. Wegscheider, L. Pfeiffer, K. West, and R. E. Leibenguth, Appl. Phys. Lett. **65**, 2510 (1994).
[39] W. Wegscheider, L. N. Pfeiffer, M. M. Dignam, A. Pinczuk, K. W. West, S. L. McCall, and R. Hull, Phys. Rev. Lett. **71**, 4071 (1993).
[40] H. Hayamizu, M. Yoshita, S. Watanabe, H. Akiyama, L. Pfeiffer, and K. West, Phys. Rev. Lett. **81**, 4937 (2002).

© 2004 WILEY-VCH Verlag GmbH & Co. KGaA, Weinheim

[41] W. Wegscheider, L. N. Pfeiffer, K. W. West, P. Littlewood, O. Narayan, M. Hagn, M. M. Dignam, and R. E. Leibenguth, Solid-State Electron. **40**, 1 (1996).
[42] G. P. Agrawal and N. K. Dutta, Long-wavelength semiconductor lasers (Van Nostrand Reinhold, New York, 1986).
[43] M. Z. Maialle, E. A. de Andrada e Silva, and L. J. Sham, Phys. Rev. B **47**, 15776 (1993).
[44] A. Vinattieri, J. Shah, T. C. Damen, D. S. Kim, L. N. Pfeiffer, M. Z. Maialle, and L. J. Sham, Phys. Rev. B **50**, 10868 (1994).
[45] L. Sorba, G. Schedelbeck, W. Wegscheider, M. Bichler, G. Böhm, and G. Abstreiter, J. Cryst. Growth **201/202**, 805 (1999).
[46] S. Sedlmaier, M. Stopa, G. Schedelbeck, W. Wegscheider, and G. Abstreiter, Phys. Rev. B **65**, 201304 (2002).
[47] W. Wegscheider, W. Kang, L. N. Pfeiffer, K. W. West, H. L. Stormer, and K. W. Baldwin, Solid-State Electron. **37**, 547 (1994).
[48] C. W. J. Beenakker and H. van Houten, in: Solid State Physics: Advances in Research and Applications, edited by H. Ehrenreich and D. Turnbull, Vol. 44 (Academic Press, New York, 1991), pp. 1–228.
[49] For reviews, see H. Kalt, Optical Properties of III–V Semiconductors (Springer-Verlag, Berlin, 1996); H. Haug and S. W. Koch, Quantum Theory of the optical and Electronic Properties of Semiconductors (World Scientific, Singapore, 1993).
[50] R. D. Grober, T. D. Harris, J. K. Trautman, E. Betzig, W. Wegscheider, L. Pfeiffer, and K. West, Appl. Phys. Lett. **64**, 1421 (1994).
[51] J. Hasen, L. N. Pfeiffer, A. Pinczuk, S. He, K. W. West, and B. S. Dennis, Nature **390**, 54 (1997).
[52] R. Ambigapathy, I. Bar-Joseph, D. Y. Oberli, S. Haacke, M. J. Brasil, F. Reinhardt, E. Kapon, and B. Deveaud, Phys. Rev. Lett. **78**, 3579 (1997).
[53] S. Das Sarma and D. W. Wang, Phys. Rev. Lett. **84**, 2010 (2000).
[54] W. Wegscheider, G. Schedelbeck, M. Bichler, and G. Abstreiter, in: Festkörperprobleme/Advances in Solid State Physics, Vol. 38, edited by B. Kramer (Vieweg, Wiesbaden, 1998), p. 153.
[55] K. Brunner, G. Abstreiter, G. Böhm, G. Tränkle, and G. Weimann, Phys. Rev. Lett. **73**, 1138 (1994).
[56] K. Brunner, G. Abstreiter, G. Böhm, G. Tränkle, and G. Weimann, Appl. Phys. Lett. **64**, 3320 (1994).
[57] D. Gammon, E. S. Snow, B. V. Shanabrook, D. S. Kratzer, and D. Park, Phys. Rev. Lett. **76**, 3005 (1996); Science **273**, 87 (1996).
[58] P. Platzman, personal communication.
[59] QDs on SL3 are to small to be resolved in this particular AFM picture shown here but were observed on the same sample by AFM with better resolution (not shown here).
[60] This is known for InAs QD growth on (001)-oriented AlGaAs, see also Ref. [10].
[61] J. G. Belk, D. W. Pashley, C. F. McConville, B. A. Joyce, and T. S. Jones, Surf. Sci. **410**, 82 (1998).
[62] D. Wasserman, S. A. Lyon, M. Hadjipanayi, A. Maciel, and J. F. Ryan, Appl. Phys. Lett. **83**, 5050 (2003).
[63] M. Yoshita, H. Akiyama, L. N. Pfeiffer, and K. W. West, Appl. Phys. Lett. **81**, 49 (2002).
[64] M. Bayer, G. Ortner, O. Stern, A. Kuther, A. A. Gorbunov, A. Forchel, P. Hawrylak, S. Fafard, K. Hinzer, T. L. Reinecke, S. N. Walck, J. P. Reithmaier, F. Klopf, and F. Schäfer, Phys. Rev. B **65**, 195315 (2002).
[65] F. Findeis, A. Zrenner, G. Böhm, and G. Abstreiter, Solid. State Comm. **114**, 227 (2000).
[66] T. Someya, H. Akiyama, and H. Sakaki, Phys. Rev. Lett. **76**, 2965 (1996).
[67] A. R. Goñi, L. N. Pfeiffer, K. W. West, A. Pinczuk, H. U. Baranger, and H. L. Stormer, Appl. Phys. Lett. **61**, 1956 (1992).
[68] D. Gershoni, J. S. Weiner, S. N. G. Chu, G. A. Baraff, J. M. Vandenberg, L. N. Pfeiffer, K. West, R. A. Logan, and T. Tanbun-Ek, Phys. Rev. Lett. **65**, 1631 (1990).
[69] H. Akiyama, T. Someya, M. Yoshita, T. Sasaki, and H. Sakaki, Phys. Rev. B **57**, 3765 (1998).
[70] J. R. Jensen, J. M. Hvam, and W. Langbein, J. Cryst. Growth **227-228**, 966 (2001).
[71] M. Grundmann, O. Stier, A. Schliwa, and D. Bimberg, Phys. Rev. B **61**, 1744 (2000).
[72] D. V. Regelman and D. Gershoni, Proceedings of the 24th International Conference on the Physics of Semiconductors, edited by D. Gershoni (World Scientific, Singapore, 1999), p. 1111.
[73] M. Sztucki, T. U. Schülli, T. H. Metzger, V. Chamard, R. Schuster, and D. Schuh, Appl. Phys. Lett. **83**, 872 (2003).
[74] W. Wegscheider, G, Schedelbeck, M. Bichler, and G. Abstreiter, phys. stat. sol. (a) **164**, 601 (1997).

© 2004 WILEY-VCH Verlag GmbH & Co. KGaA, Weinheim